

Review

Recent Advancements in Photocatalysis Coupling by External Physical Fields

Yan Mi ¹, Wenjian Fang ^{1,2,*} , Yawei Jiang ³ , Yang Yang ¹, Yongsheng Liu ³ and Wenfeng Shangguan ^{2,*}¹ School of Electrical and Energy Power Engineering, Yangzhou University, Yangzhou 225002, China² Research Center for Combustion and Environment Technology, Shanghai Jiao Tong University, Shanghai 200240, China³ Institute of Solar Energy, Shanghai University of Electric Power, Shanghai 200090, China

* Correspondence: fwjlf2227@163.com (W.F.); shangguan@sjtu.edu.cn (W.S.)

Abstract: Photocatalysis is one of the most promising green technologies to utilize solar energy for clean energy achievement and environmental governance, such as artificial photosynthesis, water splitting, pollutants degradation, etc. Despite decades of research, the performance of photocatalysis still falls far short of the requirement of 5% solar energy conversion efficiency. Combining photocatalysis with the other physical fields has been proven to be an efficient way around this barrier which can improve the performance of photocatalysis remarkably. This review will focus on the recent advances in photocatalysis coupling by external physical fields, including Thermal-coupled photocatalysis (TCP), Mechanical-coupled photocatalysis (MCP), and Electromagnetism-coupled photocatalysis (ECP). In this paper, coupling mechanisms, materials, and applications of external physical fields are reviewed. Specifically, the promotive effect on photocatalytic activity by the external fields is highlighted. This review will provide a detailed and specific reference for photocatalysis coupling by external physical fields in a deep-going way.

Keywords: photocatalysis; assisted external physical fields; coupling effects; charge separation



Citation: Mi, Y.; Fang, W.; Jiang, Y.; Yang, Y.; Liu, Y.; Shangguan, W.

Recent Advancements in Photocatalysis Coupling by External Physical Fields. *Catalysts* **2022**, *12*, 1042. <https://doi.org/10.3390/catal12091042>

Academic Editors: Detlef W. Bahnemann, Ewa Kowalska, Ioannis Konstantinou, Magdalena Janus, Vincenzo Vaiano, Wonyong Choi and Zhi Jiang

Received: 19 August 2022

Accepted: 9 September 2022

Published: 13 September 2022

Publisher's Note: MDPI stays neutral with regard to jurisdictional claims in published maps and institutional affiliations.



Copyright: © 2022 by the authors. Licensee MDPI, Basel, Switzerland. This article is an open access article distributed under the terms and conditions of the Creative Commons Attribution (CC BY) license (<https://creativecommons.org/licenses/by/4.0/>).

1. Introduction

In order to achieve the carbon emission reduction target, photocatalysis has been widely considered to be a promising technology. After half a century of development, photocatalysis has tended to increasingly mature, especially in many fields, such as pollutant degradation, water splitting, CO₂ reduction, and desulfurization [1–11]. However, the main reason limiting photocatalytic technology from basic research to practical application is that the conversion efficiency of solar energy is still very low, which is far from meeting the requirements of commercial applications [12,13]. At present, there are two main ways to break the bottleneck of the efficiency of photocatalytic energy conversion: one is to enhance the absorption rate of the solar spectrum and the other is to efficiently promote the separation of photogenerated carriers.

Techniques for modification of photocatalytic materials, such as doping, compositing other materials, cocatalyst loading, morphology controlling, etc., have been confirmed to improve light absorption and photogenerated carrier separation efficiently [14–18]. However, the energy conversion efficiency is still very low although it has been improved to some extent by these modifications. Therefore, it is necessary to find a new way to achieve a breakthrough in photocatalytic performance. Studies have shown that photocatalytic activity can be greatly improved by adding other physical fields to the photocatalytic reaction process [19,20]. Generally, the assisted external field can provide additional energy to the photocatalytic system, which will power photogenerated charge separation and thereby improve the efficiency of photocatalysis. According to the energy form, as shown in Figure 1 the assisted physical field can be divided into the thermal field, mechanical field, and, electromagnetic field. In terms of energy generation types, it can also be divided

into infrared thermal effect, microwave thermal effect, ultrasonic cavitation effect, friction electrostatic effect, external controllable electromagnetic field effect, and so on. One of the most common assisted physical fields is the thermal field. For example, in the photocatalytic reaction, most of the infrared light in the sunlight cannot be effectively used, which will dissipate into heat. Since infrared light and heat are inseparable, the infrared absorbing material can be composited into the photocatalytic material to collect the infrared band energy promoting the separation of photogenerated carriers. In addition, other non-contact external fields, such as the electric field, magnetic field, microwave field, and ultrasound field, can significantly improve the efficiency of the photocatalytic system, which have different mechanisms and respective advantages.

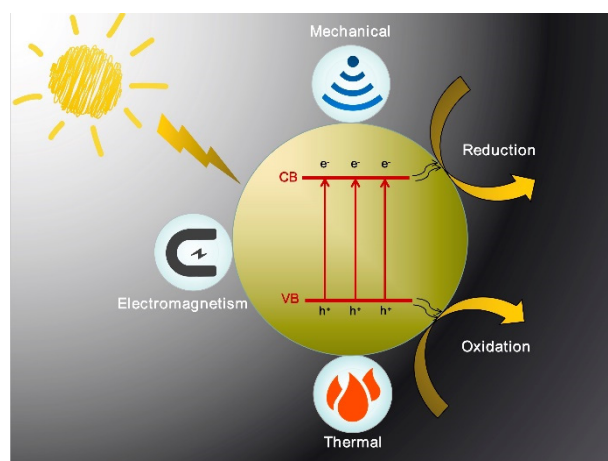


Figure 1. Schematic diagram of three types of external field-assisted photocatalysis.

Therefore, we will provide a detailed and specific reference for photocatalysis coupling by external physical fields, including thermal-coupled photocatalysis (TCP), mechanical-coupled photocatalysis (MCP), and electromagnetism-coupled photocatalysis (ECP). This paper will mainly focus on coupling mechanisms, materials, and applications of external physical fields. Specifically, the promotive effect on photocatalytic activity by the external fields will be highlighted.

2. Thermal-Coupled Photocatalysis (TCP)

To break through the existing bottleneck of photocatalytic activity, thermal energy has been introduced into photocatalysis systems. Generally, traditional photothermal catalysis can be divided into three types [19,21–27]: (1) thermal-coupled photocatalysis (TCP); (2) photo-coupled thermocatalysis (PCT); and (3) photothermal co-catalysis (PTC). As for PCT, light is not the main driving force of the reaction, which is used only to provide heat and promote the thermocatalytic process. Therefore, we will focus on the TCP and PTC, where light is the main driving force for the reaction. Compared with conventional photocatalysis, TCP can combine the advantages of thermal and light energy, thereby greatly improving photocatalytic activity. The mechanism of efficiently photocatalytic activity for TCP can be summarized as follows: (1) thermal energy may help generate electron-hole pairs; (2) thermal energy can re-emit the trapped electrons and drive them rapidly for transfer to the surface of the photocatalyst; (3) thermal energy can increase the collision rate with more efficient collisions of molecules; and (4) the high surface temperature of photocatalyst will promote the dissociative adsorption of reactant molecules. Here, we will try to summarize the current research progress of TCP including the primary source of thermal energy, materials for TCP and, the main applications of TCP.

2.1. The Primary Source of Thermal Energy

2.1.1. External Direct Heating

The simplest method to realize TCP is to introduce an external heating process through traditional heat convection, heat conduction, and heat radiation. Increasing the external temperature can inhibit the recombination of photogenerated carriers and reduce the charge transfer resistance, thereby increasing the photocatalytic reaction rate. Huang et al. synthesized $\text{Co}_{0.85}\text{Se}/\text{Mn}_{0.3}\text{Cd}_{0.7}\text{S}$ nanorods for photocatalytic H_2 production [28]. As shown in Figure 2a, the catalyst itself has no thermal catalytic activity. The H_2 production was improved with the increase in temperature. Jing et al. reported a $\text{Cu}_2\text{O-rGO}/\text{TiO}_2$ photocatalyst whose H_2 evolution rate ($17,800 \mu\text{mol g}^{-1} \text{h}^{-1}$) under the photothermal condition (90°C) is 4.7 times higher than that under only photocatalytic condition (25°C), as shown in Figure 2b [29]. The photothermal effect facilitates the separation of photogenerated electron-hole pairs and simultaneously accelerates the reaction rate on the catalyst surface during H_2 evolution. Li et al. synthesized a low-cost $\text{Cu}_2\text{O}/\text{g-C}_3\text{N}_4$ heterojunction by a simple hydrothermal method and realized efficient photothermal conversion of CO_2 into ethanol [30]. As shown in Figure 2c, under photothermal catalysis, the rate of ethanol is 1.89 times that of photocatalysis and 7.05 times that of thermocatalysis at 100°C . The temperature enhanced the thermal motion of the radical, which promotes the formation of ethanol through the CH_3 dimerization.

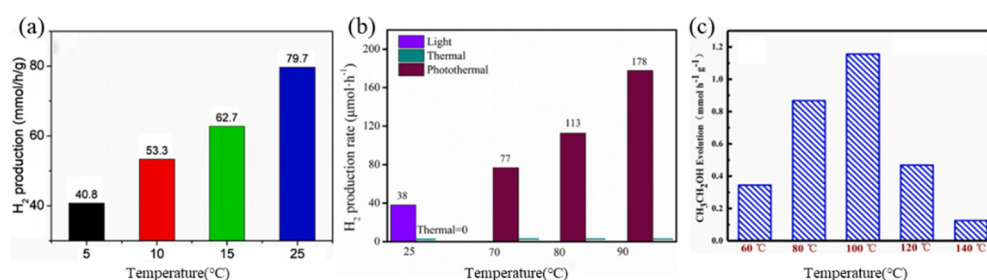


Figure 2. (a) H_2 -evolution rate of 7 wt% $\text{Co}_{0.85}\text{Se}/\text{Mn}_{0.3}\text{Cd}_{0.7}\text{S}$ at various reaction temperatures (5–25 °C) under visible light for 1 h (Reprinted/adapted with permission from Ref. [28]. Copyright 2021, copyright Elsevier). (b) H_2 production rates under light, thermal, and photothermal conditions (10 mg of 1.0% $\text{Cu}_2\text{O-rGO}/\text{TiO}_2$ was used.) (Reprinted/adapted with permission from Ref. [29]. Copyright 2022, copyright Elsevier). (c) The achieved product yield of $\text{C}_2\text{H}_6\text{O}$ over $\text{Cu}_2\text{O}/\text{g-C}_3\text{N}_4$ at different temperatures (Reprinted/adapted with permission from Ref. [30]. Copyright 2021, copyright Elsevier).

2.1.2. Near-Infrared Indirect Heating

Near-infrared indirect heating produces the photothermal effect by photothermal materials. Under near-infrared light irradiation, the absorbed photons could excite the electrons, which would migrate until they recombine with the holes. Therefore, there is an essential distinction between TCP via external direct heating and near-infrared indirect heating in terms of the way to enhance the photocatalytic activity. The photothermal effect can increase the temperature in a local area to induce a collective effect of multistage processes, which include charge excitation, charge carrier mobility, and reaction barriers. Photothermal material SnSe nanoparticles that serve as “hot islands” on ZnIn_2S_4 monolayer were proposed as an ideal model for investigating the role of the photothermal contribution in photocatalysis [31]. The energetic photoexcited electrons of nanoparticle SnSe interact with the lattice to transfer their energy to phonons for photothermal conversion. Therefore, SnSe acts as a “hot island” to release thermal energy, which increases the temperature around it. Then, the increased temperature in the local area that is caused by the photothermal effect can induce a collective effect to accelerate the photocatalytic reaction of ZnIn_2S_4 to enhance the photocatalytic performance, as shown in Figure 3. The core-shell structured WO_3/CdS photocatalyst has been reported for full-spectrum solar energy conversion. The wrapped WO_3 with abundant oxygen vacancy can store electrons activated by UV-visible

light, which can then be released by NIR light. The solar-to-hydrogen conversion efficiency under simulated solar light irradiation reaches as high as 3.00% [32]. Non-precious metal co-catalysts S vacancies 1T-WS₂, CuS, and plasmonic nanoparticles could also facilitate the driving of the photothermal effect [33,34].

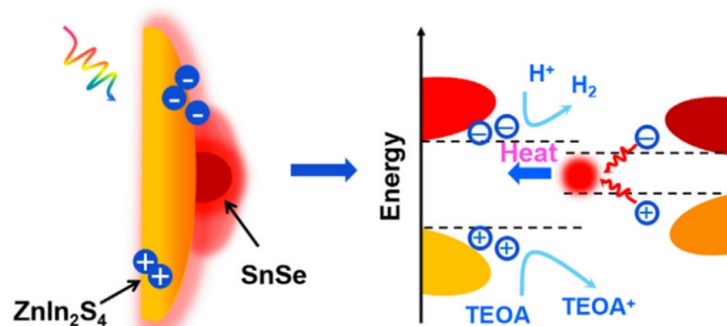


Figure 3. Schematic illustration of the photocatalytic H₂ generation process over SnSe/ZnIn₂S₄ (Reprinted/adapted with permission from Ref. [31]. Copyright 2021, copyright Elsevier).

2.1.3. Microwave Indirect Heating

The effect of microwave irradiation is a combination of thermal effects and non-thermal microwave effects, arising from the heating rate, super-heating or “hot spots”, and the selective absorption of radiation by polar substances [35,36]. Therefore, it is of great practical significance to use the coupling of microwave and UV light to improve the efficiency of photocatalytic activity. The special thermal effect generated by microwave field is different from external direct heating and near-infrared indirect heating, which shows quickly increase temperature and more uniform temperature in solution. Ling et al. have successfully prepared uniformly Ag-loaded TiO₂ for photocatalytic degradation of 4-CP and MO coupling by microwave irradiation [37]. The improved photocatalytic degradation activity of Ag/TiO₂ was due to the thermal effect and non-thermal effect. Under microwave irradiation, silver nanoparticles can not only promote the charge separation process but also enhance the adsorption of organic pollutants on the surface of TiO₂, as shown in Figure 4. Wang et al. reported a novel Z-scheme SrTiO₃/MnFe₂O₄ nanocomposite for tetracycline (TC) degradation under MW-UV exposure [38]. It has been found that the combination of MW catalytic and UV photocatalytic oxidation technologies achieves superior SrTiO₃/MnFe₂O₄ catalytic performance. The Z-scheme SrTiO₃/MnFe₂O₄ system displays high catalytic activity under MW-UV. Particularly, the generated MW plasma accelerates electron transfer and separation of e⁻-h⁺ pair, which promotes the enhancement of redox capacity and the oxidation of organics. Gayathri et al. found that the simultaneous irradiation by MW and UV is more efficient and synergistic for the mineralization of the dye compared to the respective individual energy sources [39]. The synergistic enhancement in the photocatalytic (UV/ZnO) degradation, as well as mineralization of rhodamine B (RhB) by MW, is attributed to the increased formation of reactive oxygen species (ROS) and the formation of surface defects in ZnO, which inhibits the recombination of photogenerated electrons and holes. MW can also enhance the photocatalytic degradation and mineralization of RhB even in systems with less dissolved oxygen because of the efficient transference of oxygen from the bulk of the catalyst to the surface.



Figure 4. Schematic diagram of microwave-assisted photocatalytic degradation (Reprinted/adapted with permission from Ref. [37]. Copyright 2019, copyright Elsevier).

2.2. Materials of Thermal-Coupled Photocatalysis

In thermal-coupled photocatalysis, there are three primary sources of thermal energy: external direct heating, near-infrared indirect heating, and microwave indirect heating. Generally, external direct heating and microwave indirect heating have nothing special requests for the materials. Here, we will focus on the near-infrared indirect heating materials which show a photothermal effect irradiated by near-infrared light. The surface temperature of materials will increase locally by converting solar energy into heat energy [22–24,40]. According to different photothermal conversion mechanisms (as shown in Figure 5), near-infrared light can be converted to heat by three categories of materials: (1) Metallic materials with localized surface plasmon effect; (2) Narrow-band semiconductors with non-radiative relaxation; and (3) Carbon-based materials with thermal vibration. Therefore, TCP can be realized by near-infrared indirect heating through the composite material of photocatalysts and near-infrared absorption materials.

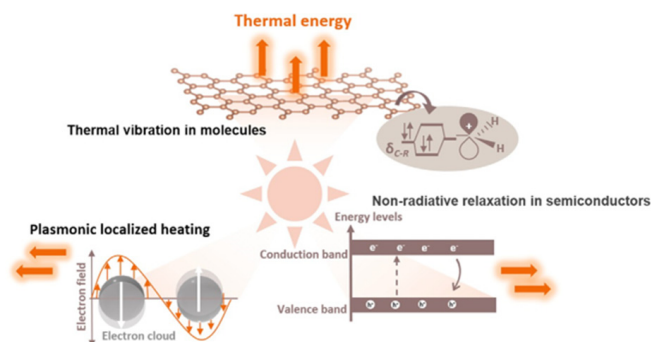


Figure 5. Schematic diagram of three photothermal effects (Reprinted/adapted with permission from Ref. [22]. Copyright 2022, copyright Elsevier).

2.2.1. Metallic Materials with Localized Surface Plasmon Effect

Under illumination, when the frequency of the light matches the resonant frequency of conduction-band electrons, electromagnetic waves can induce collective oscillations of electrons at the interface between a conducting material and a dielectric medium, such as air or water. Because it is very localized, this phenomenon is called localized surface plasmon resonance (LSPR) [41–43]. LSPR excitation can lead to a significant enhancement of the local electric field and a high concentration of energetic (hot) electrons on the surface of the plasmonic structure, a process that leads to a rapid increase in the local surface temperature of the materials. The excited hot carriers then distribute the thermal charge through electron–electron or electron–phonon scattering. Therefore, LSPR involves three distinct processes: enhancement of the local electric field, generation of hot electrons, and photothermal conversion.

The LSPR effect has been observed in many metal nanoparticles (NPs) and their alloys, such as Au, Ag, Cu, AuCu, and AuAl, etc. [44–52]. Schatz et al. investigated

the localized surface plasmon resonance (LSPR) of Cu NPs [44]. It was found that Cu shows strong and narrow LSPR peaks comparable to Ag and Au. Yan et al. reported using plasmonic Au–Pd nanostructures to directly capture visible to near-infrared light for chemical reactions [45]. The Au NPs are tightly bound to the Pd NPs for efficient light harvesting. Under plasmonic excitation, catalytic reactions are induced and accelerated through plasmonic photocatalysis and photothermal conversion. Under 809 nm laser irradiation at 1.68 W, the yield of the Suzuki coupling reaction was two times higher than when thermally heated to the same temperature. Liu et al. developed embedded coupled metal nanostructures, which proved to be an effective strategy to improve the utilization of LSPR effects (as shown in Figure 6) [46]. Compared with traditionally isolated Au nanoparticles, the contribution of Au nano chains to the enhanced light conversion rate is increased by a factor of 3.5. Ma et al. developed a series of Au–Al intermetallic compounds with a high LSPR effect [47]. The results show that the hot carrier generation rate of AuAl₂ and AuAl is higher than that of Au, and the energy rate of the resulting hot carriers is higher than that of Au. At the same time, the transport performance of hot carriers in AuAl₂ and AuAl is also better than that of Au.

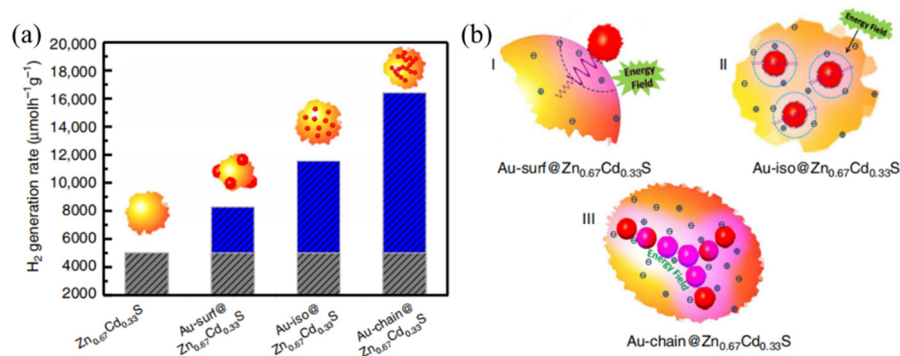


Figure 6. (a) Photocatalytic H₂ evolution activity of pure Zn_{0.67}Cd_{0.33}S and Zn_{0.67}Cd_{0.33}S supported by Au nanoparticles with different spatial arrangements (Au@Zn_{0.67}Cd_{0.33}S) under visible light irradiation (≥ 420 nm); blue columns represent the enhancement promoted by plasmonic-Au nanostructures. (b) Illustration for the proximity of semiconductors to the electromagnetic fields of plasmonic Au nanoparticles [46].

Besides metal nanoparticles, some semiconductor materials with metallic phases are also candidates for LSPR, such as CuS, Ti₃C₂, TiN, WO_{3-x}, etc. [42,53–60]. Dai et al. demonstrated the reversible displacement of surface-dependent localized surface plasmon resonances (LSPR) in CuS nanodisks [53]. As shown in Figure 7, LSPR curves (curves 1–4) shift with increasing surface-treatment cycles. Tian et al. prepared unique Cu₇S₄–Cu₉S₈ heterostructured hollow cubes with remarkable photothermal effects [55]. It is shown that the strong near-infrared plasmonic absorption of Cu₇S₄–Cu₉S₈ promotes the hot carrier transport between Cu₇S₄ and Cu₉S₈, thereby promoting the catalytic reaction. Shi et al. successfully synthesized biocompatible Ti₃C₂ nanosheets (MXenes) for cancer therapy [56]. Due to the LSPR effect of the semi-metallic Ti₃C₂ nanosheets, the ultrathin Ti₃C₂ nanosheets have strong absorption and conversion efficiency for NIR laser irradiation (808 nm). Naik et al. demonstrated that TiN is a plasmonic material in visible and near-infrared regions [57]. The research results show that TiN has comparable performance to Au in plasmonic applications, and is significantly better than gold and silver in conversion optics and other aspects. Manthiram et al. demonstrated that the metallic phase of WO_{3-x} nanoparticles possesses strong and tunable localized surface plasmon resonance [42]. Xue et al. prepared Pd-loaded plasmonic WO_{3-x} nanowires and demonstrated that the plasmon excitation of WO_{3-x} nanowires by long wavelength irradiation can greatly promote Suzuki coupling reactions catalyzed by the attached Pd nanoparticles [58].

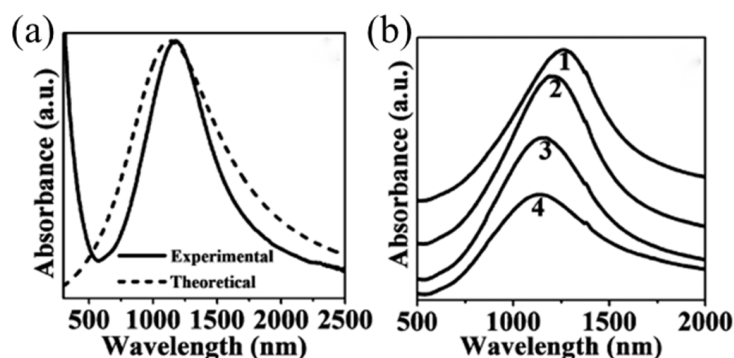


Figure 7. (a) Comparison of experimental and theoretical UV-vis-NIR absorption spectra of CuS nanodisks dispersed in tetrachloroethylene. (b) LSPR curves (curves 1–4) shift with increasing surface-treatment cycles (Reprinted/adapted with permission from Ref. [53]. Copyright 2013, copyright American Chemical Society).

2.2.2. Narrow-Band Semiconductors with Non-Radiative Relaxation

Unlike plasmonic materials, some narrow-band semiconductors generate heat through the nonradiative relaxation of electron-hole pairs. Under illumination, when the semiconductor receives energy greater than or equal to its forbidden bandwidth, electron-hole pairs are generated inside the semiconductor. Afterwards, the excited electrons and holes can relax to lower energy levels and release energy in the form of photons. Phonon relaxation leads to localized heating of the lattice and constitutes a temperature distribution that depends on its optical absorption [22,40,61].

TiO₂ is a typical representative of this photothermal conversion mechanism. Huang et al. report a large-scale production method for the synthesis of black TiO₂ by aluminum reduction, and the obtained samples have a unique crystalline core-amorphous shell structure (TiO₂@TiO_{2-x}) [62]. Under the illumination of the AM1.5G Xe lamp solar simulator, the temperature of TiO₂@TiO_{2-x} increases, which leads to more electronic excitation and relaxation and enhanced thermal emission. Black TiO₂ absorbs approximately 65% of the total solar energy through improved visible and infrared absorption. Ozin et al. synthesized black TiO_x ($x < 2$) by reducing white P25 TiO₂ nanocrystals with magnesium (Mg) [63], as shown in Figure 8a. The research results show that under the simulated illumination of 1 solar intensity, black TiO_x can effectively generate water vapor, and its photothermal conversion efficiency is as high as 50%. Yu et al. showed a slow photon effect in TiO₂ photonic crystals (TiO₂ PCs) with extraordinary photothermal effects that outperform commercial TiO₂ and TiO₂ nanotube arrays for photocatalytic methane production, as shown in Figure 8b [64]. Liu et al. proposed a novel diatom-like photothermal material using TiO₂ thin-film bilayer melamine foam (TiO₂-PANi@MF) for solar-driven clean water production [65]. The material can achieve full-spectrum light absorption and photothermal conversion. The evaporation rate of 2.12 kg m⁻² h⁻¹ was achieved under 1 sun irradiation, and the solar steam conversion efficiency was as high as 88.9%.

In addition to TiO₂, some semiconductor materials with defects also have near-infrared light-to-heat conversion properties. Chou et al. reported the NIR-photothermal properties of chemically exfoliated MoS₂ (ceMoS₂) [66]. The absorbance of ceMoS₂ in NIR is approximately 7.8 times higher than that of graphene oxide (GO). Its extinction coefficient at 800 nm is 29.2 L g⁻¹ cm⁻¹, which is higher than that of gold nanorods. Jun et al. have demonstrated for the first time that chemically exfoliated MoS₂ can be an efficient photothermal material for the creation of fresh water in solar evaporators [67]. Due to the efficient photothermal conversion of ce-MoS₂ nanosheets, the solar evaporation efficiency can reach 76% under the light intensity of 0.76 kW/m². Guo et al. proposed oxygen-deficient molybdenum oxide quantum dots (MoO_{3-x} QDs), which have an absorption spectrum matching that of sunlight in both the visible and near-infrared regions, resulting in a good interfacial heating effect on water evaporation [68]. As shown in Figure 9a, theoretical models suggest that

the unique photothermal properties of MoO_{3-x} QDs are caused by the oxygen defect level rather than the LSPR effect. Qi et al. proposed a new route to activate inert $\text{In}(\text{OH})_3$ into 2D black $\text{In}_2\text{O}_{3-x}$ nanosheets via photoinduced defect engineering, as shown in Figure 9b [69]. Due to a large number of oxygen vacancies on the layers, the black $\text{In}_2\text{O}_{3-x}$ nanosheets have a strong photothermal conversion ability. In the photothermal catalytic water gas shift experiment (RWGS), the CO production rate is as high as $103.21 \text{ mmol g}^{-1} \text{ h}^{-1}$.

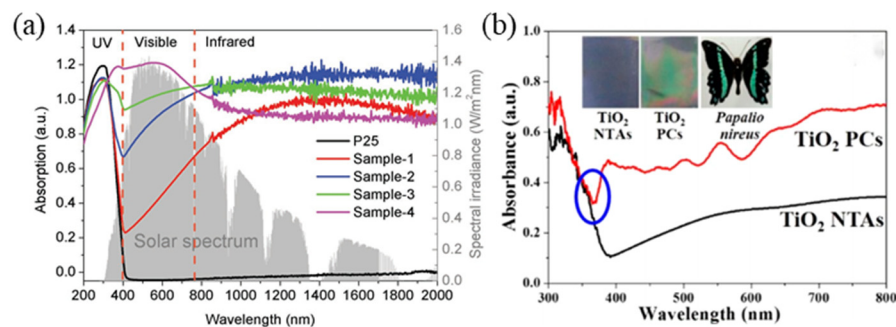


Figure 8. (a) Solar spectrum and UV-Vis-NIR absorption spectra of TiO_x nanoparticles with different colors (Reprinted/adapted with permission from Ref. [63]. Copyright 2017, copyright Wiley-VCH). (b) UV-vis absorption spectra for TiO_2 NTAs and TiO_2 PCs and the optical photograph of the TiO_2 NTAs, TiO_2 PCs, and *Papilio nireus* (Reprinted/adapted with permission from Ref. [64]. Copyright 2018, copyright American Chemical Society).

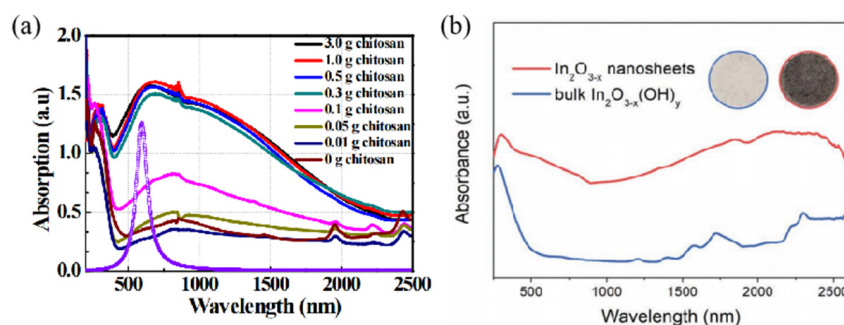


Figure 9. (a) Experimental absorption spectra of samples synthesized with different content of chitosan and simulated result by LSPR method (the dashed line) (Reprinted/adapted with permission from Ref. [68]. Copyright 2017, copyright Royal Society of Chemistry). (b) UV-vis-NIR spectra, inset: photograph (left, bulk $\text{In}_2\text{O}_{3-x}(\text{OH})_y$; right, 2D black $\text{In}_2\text{O}_{3-x}$) (Reprinted/adapted with permission from Ref. [69]. Copyright 2020, copyright Wiley-VCH).

2.2.3. Carbon-Based Materials with Thermal Vibration

Carbon-based materials have always been a research hotspot in the field of catalysis due to their excellent chemical stability and high light absorption [70,71]. Carbon-based materials possess abundant conjugated π -bonds and thus can convert solar energy into thermal energy through thermal vibration mechanisms. Under sunlight illumination, a large number of conjugated π bonds require only a small amount of energy to excite loosely held electrons, followed by electron relaxation via electron–electron and electron–phonon scattering. This causes the molecules to generate heat, which in turn causes the macroscopic heating of the material [72–74].

Carbon nanotubes (CNTs) are a classic carbon-based photothermal material. Using carbon nanotubes (CNTs) to modify flexible wood films (F-Wood/CNTs), Hu et al. created an efficient solar steam generation device [75]. Benefiting from the excellent light absorption of the black CNT coating, as shown in Figure 10a, its solar steam power generation device exhibits a high efficiency of 81% at 10 kW cm^{-2} . An all-carbon nanotube (CNT) hybrid film was prepared by Jia et al. The hybrid film has ultra-high solar absorbance, low thermal conductivity, and excellent light-to-heat conversion capability [76]. The photothermal

conversion efficiency of a single hybrid film is 87.4% under 1 sun illumination. Zhang et al. used SiO₂ nanoparticles to graft carbon nanotubes (CNTs) to prepare CNTs-SiO₂ superhydrophobic coatings [77]. Due to the superhydrophobicity of the coating surface and the remarkable photothermal conversion ability of CNTs, the CNTs-SiO₂ coating can significantly delay the water freezing time and effectively melt the ice layer within seconds under laser irradiation.

Graphene, including graphene oxide (GO) and reduced graphene oxide (rGO), has long been known for its powerful photothermal conversion capabilities. Dai et al. developed nanosheets of reduced graphene oxide (nano-rGO) with high near-infrared (NIR) absorbance, as shown in Figure 10b [78]. The single-layered nano-rGO sheets have an average lateral dimension of ~20 nm, and their NIR absorption is six times higher than that of non-reduced covalent PEGylated nano-GO. Jiang et al. synthesized two-dimensional rGO and one-dimensional multi-walled CNTs (MWCNTs) as rGO-MWCNT-based films to enhance photothermal performance [79]. The surface of the rGO-MWCNT-based film is rough, thereby reducing the reflection of light and thereby realizing almost all light trapping. Under 1 sun illumination, the surface temperature is as high as 78 °C, which is 10 °C higher than the result of pure rGO film. The solar thermal conversion efficiency can reach 80.4%. Qiu et al. prepared a reduced graphene oxide-based (rGO-based) covalent organic framework hydrogel (KTG) with a three-dimensional porous structure as a platform for enhanced uranium capture via photothermal desalination [80]. KTG can obtain a special uranium capture capacity (521.6 mg g⁻¹) under one sunlight exposure, which is 42.4% higher than that under dark conditions.

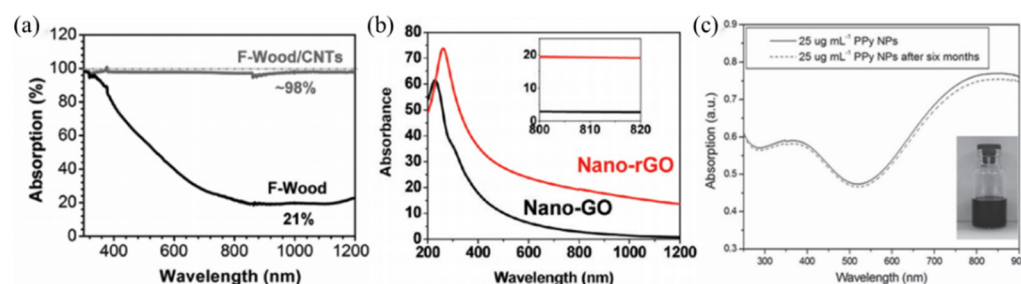


Figure 10. (a) Light absorption spectra for the F-Wood and F-Wood/CNTs membranes (Reprinted/adapted with permission from Ref. [75]. Copyright 2017, copyright Wiley-VCH). (b) UV-vis absorption curves of nano-GO and nano-rGO, respectively. The inset shows a zoom-in view of the curves in the 800 nm region (Reprinted/adapted with permission from Ref. [78]. Copyright 2011, copyright American Chemical Society). (c) UV-vis-NIR extinction spectra were recorded for 25 µg mL⁻¹ PVA stabilized PPy nanoparticles dispersed in water and stored at 4 °C for six months. The inset shows the prepared sample (Reprinted/adapted with permission from Ref. [81]. Copyright 2013, copyright Wiley-VCH).

Polymers, such as polypyrrole (PPy), and polydopamine (PDA), are also very powerful in photothermal conversion. Dai et al. constructed uniform PPy nanoparticles [81]. As shown in Figure 10c, the PPy nanoparticles have good colloidal stability and strong NIR absorption, and their photothermal conversion efficiency is better than that of the well-known Au nanorods. Jun et al. demonstrated a polydopamine (PDA)-coated polyvinylidene fluoride (PVDF) photothermal membrane for solar-driven membrane distillation [82]. The film has remarkable light absorption and excellent light-to-heat conversion performance. Under the irradiation of 0.75 kW/m², its distillation performance efficiency is 45%. Xu et al. improved light-harvesting efficiency over a wide spectral and angular range by exploiting self-organized surface structures on large-area multilayer polypyrrole (PPy) nanosheets [83]. The solar heat conversion efficiency is as high as 95.33%. In addition, when used for solar steam power generation, the measurement efficiency can reach 92% under 1 sun illumination. Chen et al. developed a porous framework photothermal microgroove-structured aerogel (PDA/PEI/PPy@PI-MS MGA, pppMGA) [84]. Combin-

ing the porous micro-grooved structure of the pppMGA evaporation interface with the light absorption ability of PPy, the light absorption rate (98%) was effectively improved. Under 1 sun illumination, the pppMGA evaporator can achieve a high evaporation rate ($\sim 1.38 \text{ kg m}^{-2} \text{ h}^{-1}$) and a high photothermal conversion efficiency ($\sim 93.04\%$).

2.3. Applications of Thermal-Coupled Photocatalysis

Thermal-coupled photocatalysis has applications in many fields, including artificial photosynthesis, water splitting, pollutant degradation, etc. The thermal-coupled photocatalysis achievements in recent years are summarized and listed in Table 1.

Table 1. Summary of thermal-coupled photocatalysis in recent years.

Material	Condition	Application	Activity	Blank Control	Ref.
SrTiO ₃ /Cu@Ni/TiN	Xe lamp (600 mW/cm ²)	artificial photosynthesis	21.33 $\mu\text{mol g}^{-1} \text{ h}^{-1}$ (C ₂ H ₆ O)	380 °C: 1.44 $\mu\text{mol g}^{-1} \text{ h}^{-1}$ (C ₂ H ₆ O)	[85]
BP/WO	300 W Xe lamp (UV-vis-NIR)	artificial photosynthesis	26.1 $\mu\text{mol g}^{-1} \text{ h}^{-1}$ (CO)	BP: 1.47 $\mu\text{mol g}^{-1} \text{ h}^{-1}$ (CO)	[86]
Au-MgO/TiO ₂	300 W Xe lamp (UV-vis-NIR)	artificial photosynthesis	6.624 $\mu\text{mol g}^{-1} \text{ h}^{-1}$ (CH ₄)	P25: 2.07 $\mu\text{mol g}^{-1} \text{ h}^{-1}$ (CH ₄)	[87]
La _{0.4} Pr _{0.6} Mn _{0.6} Ni _{0.4} O _{3-δ}	300 W Xe lamp ET: 300 °C	artificial photosynthesis	3970 $\mu\text{mol g}^{-1} \text{ h}^{-1}$ (CH ₄ O)	PC: 0.24 $\mu\text{mol g}^{-1} \text{ h}^{-1}$ (CH ₄ O)	[88]
CoO-CuO/TiO ₂ - CeO ₂	300 W Xe lamp	artificial photosynthesis	1.84 $\mu\text{mol g}^{-1} \text{ h}^{-1}$ (CH ₄)	PC: 0.5 $\mu\text{mol g}^{-1} \text{ h}^{-1}$ (CH ₄)	[89]
Cu:CsPbBr ₃	300 W Xe lamp	artificial photosynthesis	14.72 $\mu\text{mol g}^{-1} \text{ h}^{-1}$ (CH ₄)	CsPbBr ₃ : 3.62 $\mu\text{mol g}^{-1} \text{ h}^{-1}$ (CH ₄)	[90]
Cu ⁰ /Cu ₂ O	300 W Xe lamp ($\lambda > 400 \text{ nm}$)	artificial photosynthesis	2.6 $\mu\text{mol g}^{-1} \text{ h}^{-1}$ (CH ₄ O)	Cu ₂ O: 0 $\mu\text{mol g}^{-1} \text{ h}^{-1}$ (CH ₄ O)	[91]
Cs ₃ Sb ₂ I ₉	Xe lamp (200 mW/cm ²) ET: 235 °C	artificial photosynthesis	95.7 $\mu\text{mol g}^{-1} \text{ h}^{-1}$ (CO)	PC: 1.1 $\mu\text{mol g}^{-1} \text{ h}^{-1}$ (CO)	[92]
Bi ₂ O _{3-x}	LED light (365–940 nm)	artificial photosynthesis	AQY = 0.113% (940 nm)	AOY = 0.028% (450 nm)	[93]
Au/rutile	300 W Xe lamp (UV-vis-NIR)	artificial photosynthesis	$\sim 5 \mu\text{mol g}^{-1} \text{ h}^{-1}$ (CO)	rutile: $\sim 2.25 \mu\text{mol g}^{-1} \text{ h}^{-1}$ (CO)	[94]
TiO ₂ (AB)	150 W Xe lamp (UV-vis-NIR)	artificial photosynthesis	11.93 $\mu\text{mol g}^{-1} \text{ h}^{-1}$ (CH ₄)	PC: 0.09 $\mu\text{mol g}^{-1} \text{ h}^{-1}$ (CH ₄)	[95]
AuCu/g-C ₃ N ₄	300 W Xe lamp ET: 120 °C	artificial photosynthesis	0.89 mmol g ⁻¹ h ⁻¹ (C ₂ H ₆ O)	PC: 0.21 mmol g ⁻¹ h ⁻¹ (C ₂ H ₆ O)	[49]
Cu ₂ O/g-C ₃ N ₄	300 W Xe lamp ($\lambda > 420 \text{ nm}$) ET: 100 °C	artificial photosynthesis	0.71 mmol g ⁻¹ h ⁻¹ (C ₂ H ₆ O)	PC: 0.37 mmol g ⁻¹ h ⁻¹ (C ₂ H ₆ O)	[30]

Table 1. Cont.

Material	Condition	Application	Activity	Blank Control	Ref.
Ag-PDA/DCN	300 W Xe lamp ($\lambda > 420$ nm)	H ₂ production	3840 $\mu\text{mol g}^{-1} \text{h}^{-1}$	PDA/DCN: 548 $\mu\text{mol g}^{-1} \text{h}^{-1}$	[96]
1T-WS ₂ /CdS	300 W Xe lamp ($\lambda > 420$ nm)	H ₂ production	70.9 mmol g ⁻¹ h ⁻¹	Pt _{0.02} -CdS: 20.2 mmol g ⁻¹ h ⁻¹	[33]
TiO ₂ @CS	300 W Xe lamp ET: 120 °C	H ₂ production	22772.6 $\mu\text{mol g}^{-1} \text{h}^{-1}$	120 °C: ~1100 $\mu\text{mol g}^{-1} \text{h}^{-1}$	[71]
RuO ₂ /TiO ₂ /Pt/C	300 W Xe lamp ($\lambda > 420$ nm)	H ₂ production	81.62 $\mu\text{mol g}^{-1} \text{h}^{-1}$	RuO ₂ -Pt/TiO ₂ /C: 37.45 $\mu\text{mol g}^{-1} \text{h}^{-1}$	[97]
Cu ₂ O-rGO/TiO ₂	300 W Xe lamp ET: 90 °C	H ₂ production	17.8 mmol g ⁻¹ h ⁻¹	PC: 3.8 mmol g ⁻¹ h ⁻¹	[29]
Pt/ZnIn ₂ S ₄	300 W Xe lamp (200 mW/cm ²)	H ₂ production	19.4 mmol g ⁻¹ h ⁻¹	Co ₉ S ₈ @ZnIn ₂ S ₄ : 6.25 mmol g ⁻¹ h ⁻¹	[98]
oxide-MoS ₂	Xe lamps	H ₂ production	7.85 mmol g ⁻¹ h ⁻¹	2H-MoS ₂ : 2.52 mmol g ⁻¹ h ⁻¹	[99]
C@TiO ₂ /TiO _{2-x}	300 W Xe lamp ET: 80 °C	H ₂ production	3667 $\mu\text{mol g}^{-1} \text{h}^{-1}$	TiO _{2-x} : 262 $\mu\text{mol g}^{-1} \text{h}^{-1}$	[100]
SAAg-g-CN	300 W Xe lamp ET: 55 °C	H ₂ production	498 $\mu\text{mol g}^{-1} \text{h}^{-1}$	25 °C: 248 $\mu\text{mol g}^{-1} \text{h}^{-1}$	[101]
FeS ₂ /Bi ₂ S ₃	300 W Xe lamp	H ₂ production	16.8 mmol g ⁻¹ h ⁻¹	FeS ₂ : 0.52 mmol g ⁻¹ h ⁻¹	[102]
wood/CuS-MoS ₂	AM 1.5 G (100 mW/cm ²)	H ₂ production	85604 $\mu\text{mol g}^{-1} \text{h}^{-1}$	MoS _x -TiO ₂ : 11090 $\mu\text{mol g}^{-1} \text{h}^{-1}$	[103]
Ag@SiO ₂ @TiO ₂ /Au	UV LED (365 nm) (150 mW/cm ²)	H ₂ production	30.2 mmol g ⁻¹ h ⁻¹	SiO ₂ @TiO ₂ : 0.41 mmol g ⁻¹ h ⁻¹	[104]
SnSe/ZnIn ₂ S ₄	300 W Xe lamp (UV-vis-NIR)	H ₂ production	5058 $\mu\text{mol g}^{-1} \text{h}^{-1}$	ZnIn ₂ S ₄ : 1691 $\mu\text{mol g}^{-1} \text{h}^{-1}$	[31]
Co _{0.85} Se/Mn _{0.3} Cd _{0.7} S	300 W Xe lamp ($\lambda > 420$ nm) ET: 25 °C	H ₂ production	79.7 mmol g ⁻¹ h ⁻¹	5 °C: 46.7 mmol g ⁻¹ h ⁻¹	[28]
Ni ₂ P/TiO ₂ (B)	300 W Xe lamp ET: 90 °C	H ₂ production	20.129 mmol g ⁻¹ h ⁻¹	50 °C: 6.752 mmol g ⁻¹ h ⁻¹	[105]
Au/SiO ₂ /CdS/Ag	LEDs (400–800 nm)	H ₂ production	130 mmol g ⁻¹ h ⁻¹	SiO ₂ /CdS/Ag: 37.53 mmol g ⁻¹ h ⁻¹	[106]
WO ₃ /CdS	300 W Xe lamp (UV-vis-NIR)	H ₂ production	65.98 mmol g ⁻¹ h ⁻¹	10 °C: 20.82 mmol g ⁻¹ h ⁻¹	[32]
Zn NPs	halogen lamp (4.67 W/cm ²)	H ₂ production	200 $\mu\text{mol g}^{-1} \text{h}^{-1}$	Zn powder: 20 $\mu\text{mol g}^{-1} \text{h}^{-1}$	[107]
PVDF-HFP/CdS/CNT	280 W Xe lamp	H ₂ production	451 $\mu\text{mol g}^{-1} \text{h}^{-1}$	PVDF-CTFE/CdS: 136 $\mu\text{mol g}^{-1} \text{h}^{-1}$	[108]
PDA/DCN	Xe lamp ($\lambda > 420$ nm)	MB degradation	DE = 98% (70 min)	DCN: DE = 48%	[109]

Table 1. Cont.

Material	Condition	Application	Activity	Blank Control	Ref.
Cu _{0.75} Ag _{0.5} S	300 W Xe lamp	MB degradation	DE = 93.8% (30 min)	CuS/rGO: DE = 80% (140 min)	[110]
CuFe ₂ O ₄ @MIL-100(Fe, Cu)	300 W Xe lamp (λ > 400 nm)	MB degradation	k = 0.075 min ⁻¹	CuFe ₂ O ₄ : k = 0.023 min ⁻¹	[111]
Prussian blue (PB) microcrystals	solar simulator (100 mW/cm ²)	MB degradation	k = 0.0430 min ⁻¹	PC: k = 0.0231 min ⁻¹	[112]
C@TiO ₂	300 W Xe lamp	RhB degradation	k = 0.045 min ⁻¹	TiO ₂ MNF: k = 0.011 min ⁻¹	[113]
OPTCu-NCs	808 nm NIR laser	RhB degradation	DE = 91.87% (120 min)	-	[114]
CoFe ₂ O ₄ -BiOCl	300 W Xe lamp	RhB degradation	k = 1.16 min ⁻¹	Vis: k = 0.74 min ⁻¹	[115]
ZnSnO ₃	UV light (293–338 K)	RhB degradation	DE = 98.1% (80 min)	UV: DE = 76.8%	[116]
ZnO	6 W mercury arc lamp	RhB degradation	DE ≈ 75% (30 min)	PC: DE ≈ 50%	[39]
Au/TiO ₂ _PW	300 W Xe lamp (UV-vis light)	MO degradation	DE = 74% (30 min)	Au-TiO ₂ : DE = 10%	[117]
TiX _n	150 W Xe lamp	MO degradation	DE = 90% (120 min)	TiS ₃ : DE = 34% (180 min)	[118]
Ag/TiO ₂	300 W Hg lamp	MO degradation	DE = 100% (60 min)	-	[37]
Fe ₃ O ₄ @SiO ₂ -laccase	500 W Xe lamp (λ > 400 nm)	MG degradation	DE = 99.6% (60 min)	alizarin red: DE = 79.3%	[119]
Pt–Cu/TiO ₂	300 W Xe lamp	toluene degradation	DE = ~100% (120 min)	110 °C: DE = ~1%	[120]
WO _{3-x} -R/GdCrO ₃	Xe lamp (400 mW/cm ²)	toluene degradation	k = 0.029 min ⁻¹	SrTiO ₃ /TiO ₂ : k = 0.0054 min ⁻¹	[121]
Pt/[TiN@TiO ₂]	Xe lamp (500 mW/cm ²)	toluene degradation	DE = 100% (24 min)	Pt/TiO ₂ : DE = ~45%	[122]
SmMnO ₃ /CuMnO _x	400 W Xe lamp (λ > 420 nm)	toluene degradation	DE = 100% (275 °C)	SmMnO ₃ : DE = 100% (300 °C)	[123]
LaMn _{1.3} O ₃	300 W Xe lamp (94 mW/cm ²)	toluene degradation	DE = 98% (120 min)	-	[124]
Cu/TiO _{2-x} /CoP	300 W Xe lamp	2,4-D degradation	DE = 99.2% (180 min)	TiO _{2-x} /CoP: DE = 75.8%	[125]
Ag/Bi ₂ S ₃ /MoS ₂	500 W Xe lamp (λ > 420 nm)	2,4-D degradation	k = 0.02334 min ⁻¹	Bi ₂ S ₃ /MoS ₂ : k = 0.00638 min ⁻¹	[126]
Cu _{2-x} S/CdS/Bi ₂ S ₃	300 W Xe lamp (λ > 420 nm)	2,4-D degradation	k = 0.03193 min ⁻¹	Cu _{2-x} S/Bi ₂ S ₃ : k = 0.00422 min ⁻¹	[127]
α-Fe ₂ O ₃ /Defective MoS ₂ /Ag	Xe lamp (λ > 420 nm)	2,4-D degradation	k = 0.043 min ⁻¹	α-Fe ₂ O ₃ : k = 0.0013 min ⁻¹	[128]
TiO ₂	200 W mercury lamp	2,4-D degradation	k ≈ 0.007 min ⁻¹ (O ³)	PC: k ≈ 0.001 min ⁻¹	[129]

Table 1. Cont.

Material	Condition	Application	Activity	Blank Control	Ref.
$W_{18}O_{49}@ZnIn_2S_4/CC$	300 W Xe lamp ($\lambda > 420$ nm)	BPA degradation	DE = 95% (150 min)	CC: DE = 15%	[130]
Ag/NaCNN/NiFe-LDH	500 W Xe lamp ($\lambda > 420$ nm)	BPA degradation	$k = 0.0432 \text{ min}^{-1}$	NiFe-LDH: $k = 0.00292 \text{ min}^{-1}$	[51]
$Cu_{2-x}S/Fe-POMs/AgVO_3$	300 W Xe lamp ($\lambda > 420$ nm)	BPA degradation	DE = 98.6% (150 min)	AgVO ₃ : DE = 19.6%	[131]
$Bi_7O_9I_3/AgI$	Xe lamp ($\lambda > 420$ nm)	phenol degradation	DE = 95.38% (80 min)	$Bi_7O_9I_3$: DE = 30.1%	[132]
$Bi_{12}CoO_{20}$	300 W Xe lamp ET: 90 °C	phenol degradation	$k = 0.113 \text{ min}^{-1}$	15 °C: $k = 0.009 \text{ min}^{-1}$	[133]
AuAgPt-12 YSNSs	500 W Xe lamp	4-NP degradation	$k = 0.155 \text{ min}^{-1}$	AuAgPt-6 YSNSs: $k = 0.023 \text{ min}^{-1}$	[134]
$CaCO_3/CuS$	NIR laser (2.5 W/cm ²)	4-NP degradation	DE = 98% (15 min)	CuS NPs: DE = 0%	[34]
$SrTiO_3/MnFe_2O_4$	200 W low-pressure Hg lamp	TC degradation	DE = 100% (20 min)	PC: DE = 38.2% (25 min)	[38]
$ZnO-MnO_2$	300 W Xe lamp	TC degradation	$k \approx 0.23 \text{ min}^{-1}$	MnO_2 : $k \approx 0.2 \text{ min}^{-1}$	[135]
Ag/Ag ₃ PO ₄ /CeO ₂	300 W Xe lamp	benzene degradation	DE = 90.18% (180 min)	CeO ₂ : DE \approx 70%	[136]
$\alpha-MnO_2/GO$	300 W Xe lamp	formaldehyde degradation	DE = 100% (60 min)	-	[137]
Co_3O_4/rGO	500 W Xe lamp (UV-vis-NIR)	fethanol degradation	DE = 96% (90 min)	UV-vis: DE = 41%	[138]
$ZnFe_2O_4$	MEDL MW oven (100 W)	TCH degradation	DE = 91.6% (250 s)	PC: DE \approx 20%	[139]
TiO ₂	UV lamps	4C2AP degradation	DE = 93.23% (30 min)	PC: DE = 85.28%	[140]

ET: external heating temperature; PC: photocatalysis; DE: degradation efficiency; k: degradation rate constant; MEDL: microwave electrodeless discharge lamp; MW: microwave; MB: methylene blue; RhB: rhodamine B; MO: methyl orange; MG: malachite green; 2,4-D: 2,4-dichlorophenol; BPA: bisphenol A; 4-NP:4-nitrophenol; TC: tetracycline; TCH: tetracycline hydrochloride; 4C2AP: 4-chloro 2-aminophenol.

2.3.1. Artificial Photosynthesis

Photosynthesis is one of the most important reactions on Earth. Artificial photosynthesis attempts to replicate natural photosynthesis, thereby achieving the goal of reducing CO₂. Artificial photosynthesis can simply be defined as the process of converting CO₂ and water into carbon-based fuels under sunlight [141–143]. Products from CO₂ reduction include CH₄, CO, methanol, methane, etc. However, the single photocatalytic method suffers from disadvantages, such as low charge separation efficiency, poor light-harvesting ability, and less reduction selectivity. In contrast, thermal-coupled photocatalysis couples solar and thermal energy, providing a more reliable solution.

Combining the photocatalytic properties of TiO₂ with the thermocatalytic properties of CeO₂, Fiorenza et al. synthesized TiO₂-CeO₂-based catalysts for artificial photosynthesis [89]. Furthermore, the addition of Co-Cu oxide increases the number of oxygen vacancies, which facilitates the separation of carriers. As shown in Figure 11, under the combined action of thermal energy and solar energy, the CO and CH₄ yields can reach 12 $\mu\text{mol g}^{-1} \text{ h}^{-1}$ and 1.84 $\mu\text{mol g}^{-1} \text{ h}^{-1}$, respectively. Xuan et al. designed SrTiO₃/Cu@Ni/TiN catalysts for CO₂ reduction to ethanol [85]. Non-noble metallic materi-

als, such as Cu, Ni, and TiN were used to enhance the plasmonic effect for efficiently capturing solar full-spectrum energy. The optimal ethanol evolution rate is $21.3 \mu\text{mol g}^{-1} \text{h}^{-1}$, and the ethanol selectivity is 79%. Lou et al. constructed a plasmonic semiconductor heterostructure photocatalyst with pyroelectric black phosphorus (BP) and plasmonic tungsten oxide (WO) for artificial photosynthesis [86]. Under the irradiation of visible light and NIR light, the plasmonic thermal effect of WO can increase the local temperature to $86 \text{ }^\circ\text{C}$, triggering the pyroelectric effect of BP, generating pyroelectric carriers, and enhancing the electron transfer from BP to WO. Thus, the photothermal catalytic performance is enhanced. Its CO generation reaches $26.1 \mu\text{mol g}^{-1} \text{h}^{-1}$, which is 7 times and 17 times that of plasma WO and pyroelectric BP, respectively. Xu et al. developed a novel lead-free perovskite $\text{Cs}_3\text{Sb}_2\text{I}_9$ photocatalyst to efficiently reduce CO_2 to CO and methane via photothermal co-catalysis [92]. Its optimal production rate is $95.7 \mu\text{mol g}^{-1} \text{h}^{-1}$, which is 87 times and 5.2 times higher than that of pure photocatalysis and pure thermal catalysis, respectively. The study found that the defective active sites generated by thermal excitation of $\text{Cs}_3\text{Sb}_2\text{I}_9$ photocatalysts can adsorb and activate CO_2 , while the large number of electrons excited by light can provide CO_2 reduction ability, and their synergistic effect enhances the catalytic activity. Cui et al. reported ultrathin porous $\text{g-C}_3\text{N}_4$ nanosheets decorated with AuCu alloy NPs for photothermal catalytic CO_2 reduction to ethanol [49]. The strong interaction between metal and $\text{g-C}_3\text{N}_4$ accelerates the transfer of photogenerated charges. In addition, the increase in temperature leads to enhanced thermal motion of molecules, leading to a synergistic effect of photocatalysis and thermocatalysis. At $120 \text{ }^\circ\text{C}$, the yield and selectivity of ethanol is $0.89 \text{ mmol g}^{-1} \text{h}^{-1}$, which is 4.2 times higher than that of photocatalysis and 7.6 times higher than that of thermal catalysis.

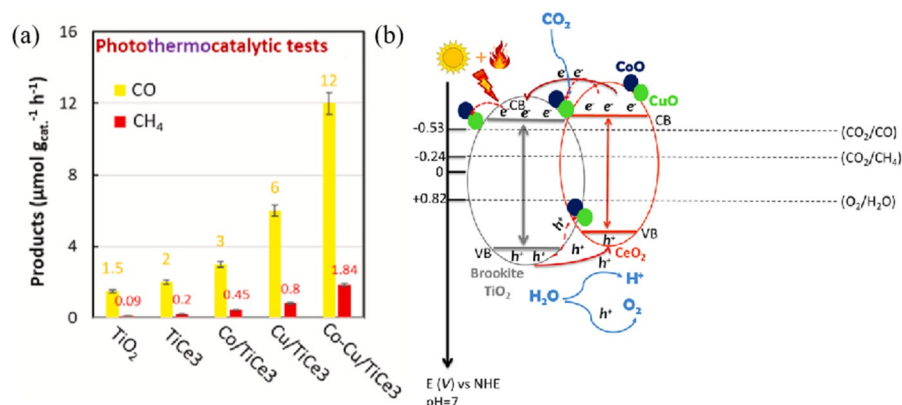


Figure 11. (a) Photothermal catalytic performances at $T = 120 \text{ }^\circ\text{C}$ on the $\text{TiO}_2\text{-CeO}_2$ -based samples. (b) Photothermal catalytic mechanism with the $\text{CoO-CuO/TiO}_2\text{-CeO}_2$ catalyst (Reprinted/adapted with permission from Ref. [89]. Copyright 2022, copyright Elsevier).

2.3.2. Water Splitting

To effectively solve the consumption of fossil fuels and the serious environmental problems that accompany combustion, modern society has been looking for a clean, renewable, and cheap energy production method. Solar-driven photocatalytic water splitting for H_2 production is a potentially effective solution to the energy crisis, especially with few environmental concerns [144–146]. However, there are widespread problems in photocatalytic water splitting for H_2 production, including low solar energy utilization efficiency, poor response to visible and infrared light, and rapid recombination of photogenerated electrons and holes. To improve these problems, introducing thermal energy into a photocatalytic H_2 production system has become a research hotspot.

Li et al. prepared Ag-polydopamine nanoparticles co-decorated defective mesoporous carbon nitride nanosheet assemblies (Ag-PDA/DCN) [96]. The photocatalytic H_2 evolution rate of this material is as high as $3840 \mu\text{mol g}^{-1} \text{h}^{-1}$, driven by visible and near-infrared light, which is seven times higher than that of PDA/DCN. This is mainly due to the rapid

electron transfer achieved by Ag-PDA nanoparticles, which further expands the photore-sponse of DCN, resulting in an obvious photothermal effect, which further enhances the photocatalytic activity. Yu et al. used an S-vacancy 1T-WS₂ (Vs-1T-WS₂) as a photothermal co-catalyst and complexed it with CdS to promote photocatalytic H₂ evolution [33]. The catalyst can achieve H₂ evolution performance of 70.9 mmol g⁻¹ h⁻¹ at 500 nm with an apparent quantum yield (AQY) of 39.1%. The introduction of Vs-1T-WS₂ not only expanded the light absorption range but also accelerated the directional migration of electrons from CdS to S vacancies through the induced photothermal effect. Guo et al. proposed an efficient two-phase photocatalytic H₂ production system [103]. The system uses a charred wood substrate to convert liquid water into water vapor and split the water vapor into H₂ in the presence of light without additional energy. The particle photocatalytic system based on the wood/CoO system achieved H₂ production rate as high as 220.74 μmol h⁻¹ cm⁻², indicating that the photothermal-photocatalytic biphasic system is cost-effective and beneficial for practical applications. Ho et al. have successfully synthesized Ag@SiO₂@TiO₂/Au catalysts with dual effects of enhanced charge transfer and photothermal heating for photo-splitting water for H₂ production (as shown in Figure 12) [104]. The catalyst has an extremely high H₂ generation rate of 30.2 mmol g⁻¹ h⁻¹. Ag@SiO₂ absorbs visible light for efficient photothermal conversion, thereby promoting the increase in the number of active sites for photocatalytic reactions. The Au Nps reduced the charge recombination in TiO₂ and further enhanced the photocatalytic performance. Jiang et al. reported the incorporation of single-atom silver into g-C₃N₄ (SAAg-g-CN) as a low-cost and efficient photocatalyst [101]. The unique coordination of SAAg-g-CN can shorten the electron transfer pathway and facilitate H₂ desorption, thereby advancing the photocatalytic H₂ production process. Furthermore, the strong N-Ag covalent bond masks the weakness of the metal NP cocatalyst in terms of growth and agglomeration under high-temperature reactions, ensuring the remarkable performance of SAAg-g-CN in thermal-assisted photocatalytic H₂ production. The average H₂ evolution rate (75 μmol g⁻¹ h⁻¹) of this catalyst is nine times that of g-C₃N₄.

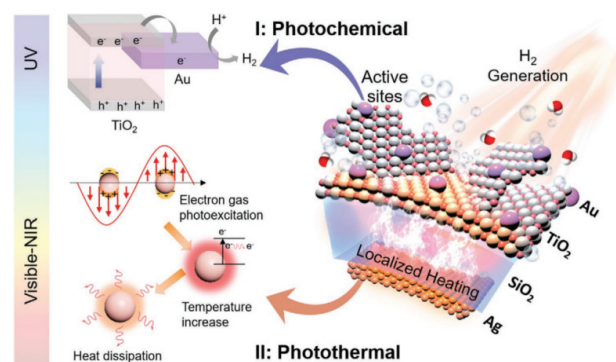


Figure 12. The schematic diagram illustrates the mechanism for enhanced photocatalytic H₂ generation due to photothermal and photochemical effects (Reprinted/adapted with permission from Ref. [104]. Copyright 2021, copyright Wiley-VCH).

2.3.3. Pollutants Degradation

Organic dyes are the most notorious pollutants in the aquatic environment. The low-cost degradation of organic fuels is of great significance in industrial production. Thermal-coupled photocatalysis degradation of organic pollutants is low-cost and can be performed under mild conditions, so it is considered a promising technology. At present, researchers have made more research results on the degradation of common organic dyes, such as methylene blue (MB) [109–112], rhodamine B (RhB) [113–116], and methyl orange (MO) [117,118], etc. Zhou et al. prepared a polydopamine/defective ultrathin mesoporous graphitic carbon nitride (PDA/DCN) Z-scheme organic assembly [109]. Under the light, the removal rate of MB was as high as 98% within 70 min. PDA extends the photore-

sponse to the near-infrared region and produces a pronounced photothermal effect, thereby enhancing the catalytic performance. Bao et al. fabricated CoFe_2O_4 -modified BiOCl layered microspheres (CFO-BiOCl) [115]. The CFO-BiOCl sample has obvious photothermal catalytic activity, decomposing 99% of RhB within 5 min under full-spectrum light irradiation. Its excellent photocatalytic performance can be attributed to the suitable band arrangement of CoFe_2O_4 and BiOCl as well as the photothermal effect, which elevates the organic pollutant molecules to a more active state (as shown in Figure 13). Tian et al. integrated porous Au/TiO_2 with butterfly *P. paris*'s wings (PW) as an Au/TiO_2 _PW photocatalyst [117]. The Au NPs enhanced the photothermal effect of the catalyst, and the PW could adjust the temperature, thus avoiding overheating and reducing the catalytic activity. The material exhibits excellent MO degradation performance due to the synergistic effect between photothermal and photocatalysis. Due to the synergistic effect of photothermal and photocatalysis, the degradation rate of MO was 74.2% within 30 min, which was 3.4 times that of TiO_2 .

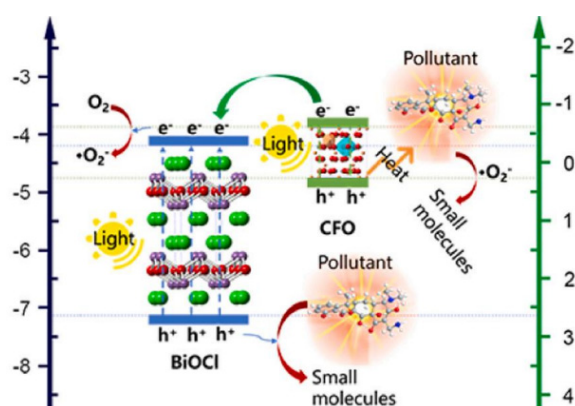


Figure 13. Schematic diagram of the photothermal catalytic mechanism of CFO-BiOCl (Reprinted/adapted with permission from Ref. [115]. Copyright 2021, copyright Elsevier).

Volatile organic compounds (VOCs) are the main air pollutants on the earth, which have great harm to human health and the environment. At present, the thermal-coupled photocatalysis degradation of VOCs has made great progress. Common VOCs, including toluene [120–124], benzene [136], phenol [132,133], and 2,4-dichlorophenol [125–128], be efficiently degraded under thermal-coupled photocatalysis. Jiang et al. investigated the performance of Pt–Cu/ TiO_2 nanocatalysts for photo–thermal catalytic degradation of toluene [120]. The photothermal effect of PtCu alloy nanoparticles and the photocatalysis of TiO_2 induced a synergistic effect (as shown in Figure 14), which resulted in a higher efficiency of toluene degradation than the thermocatalytic or photocatalytic process. At 110 °C, the toluene degradation rate is close to 100%. Li et al. prepared Z-scheme $\text{Ag}/\text{Ag}_3\text{PO}_4/\text{CeO}_2$ heterojunction photothermal catalysts for gaseous benzene degradation [136]. At the initial benzene concentration of 600 ppm, the removal rate after 3 h was 90.18%. Ag_3PO_4 has better solar light absorption ability and CeO_2 has a good thermal conductivity at lower temperatures. Under illumination, the photothermal effect promotes the efficient separation of photoexcited electrons and holes. Zhu et al. successfully prepared a photothermal catalyst $\text{Bi}_{12}\text{CoO}_{20}$ with wide spectrum adsorption (up to 1000 nm) [133]. The photothermal effect leads to the conversion of Co^{3+} and Bi^{3+} to Co^{2+} and Bi^{5+} at the octahedral site, which promotes charge separation. The catalyst has a high photothermal activity for the degradation of phenols, which is 2–8 times higher than the reported $\text{Bi}_{25}\text{CoO}_{40}$, P25- TiO_2 , g- C_3N_4 , and Bi_2WO_6 . A layered heterojunction photocatalyst $\text{Cu}/\text{TiO}_{2-x}/\text{CoP}$ was prepared by Xing et al. [125]. The LSPR effect of Cu NPs enables the catalyst to have a significant photothermal effect, thus exhibiting good photothermal-photocatalytic performance. It has a high photocatalytic degradation rate for 2,4-dichlorophenol (99.2%), which is 7.6 times that of the initial TiO_2 .

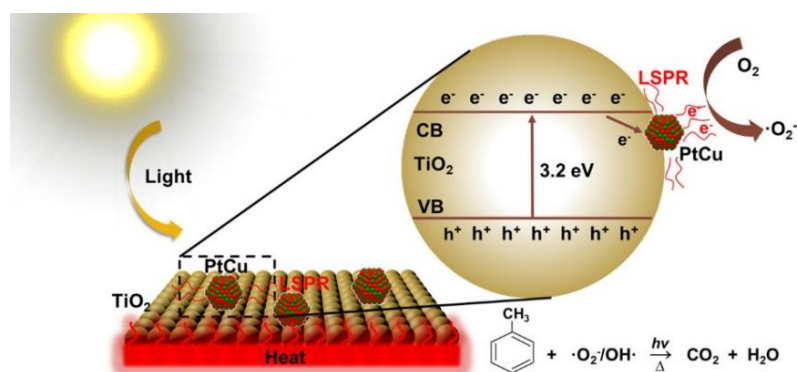


Figure 14. Mechanistic diagram of the photo–thermal catalytic degradation of the toluene reaction on Pt–Cu/TiO₂ catalysts (Reprinted/adapted with permission from Ref. [120]. Copyright 2022, copyright American Chemical Society).

In addition to the above organic pollutants, thermal-coupled photocatalysis can also be used for the degradation of bisphenol A (BPA), formaldehyde, etc. Xing et al. fabricated flower-like hollow W₁₈O₄₉@ZnIn₂S₄ core-shell Z-type heterojunctions on carbon fiber cloth (CC) [130]. The catalyst showed good photocatalytic degradation performance for the degradation of bisphenol A (BPA) under simulated sunlight, and the removal rate of bisphenol A (BPA) was 95%. α -MnO₂/graphene oxide nanohybrid was prepared by Rong et al. [137]. The catalyst can decompose 100% of formaldehyde at room temperature. On the one hand, the addition of graphene oxide is beneficial to improving the light absorption capacity and photothermal conversion efficiency; on the other hand, it is beneficial to electron transfer and separation of electrons and holes. These synergistic effects significantly enhance the catalytic activity of α -MnO₂/graphene oxide nanohybrid.

3. Mechanical-Coupled Photocatalysis (MCP)

Noncentrosymmetric materials with spontaneous polarization, ferroelectric polarization, or piezoelectric polarization can be used to utilize mechanical energy. For example, when a piezoelectric material is subjected to compressive stress or tensile stress, the material will deform and a built-in electric field with different directions will be generated. This piezoelectric effect has been utilized in the field of photocatalysis to further improve photocatalytic efficiency. Generally, external forces are applied by ultrasound, stirring, and so on. Here, we will try to summarize the current research progress of MCP including the primary source of mechanical energy and materials for MCP. In addition, we also list the application results of mechanical-coupled photocatalysis in recent years in Table 2.

Table 2. Summary of mechanical-coupled photocatalysis in recent years.

Material	Condition	Application	Activity	Blank Control	Ref.
BaTiO ₃ @C	300 W Xe lamp 40 kHz US cleaner	RhB degradation	$k = 0.03585 \text{ min}^{-1}$	PZC: $k = 0.00085 \text{ min}^{-1}$	[147]
Ag@Na _{0.5} Bi _{0.5} TiO ₃	300 W Xe lamp 40 kHz US cleaner	RhB degradation	$k = 0.146 \text{ min}^{-1}$	Na _{0.5} Bi _{0.5} TiO ₃ (PC): $k = 0.019 \text{ min}^{-1}$	[148]
Bi ₂ WO ₆ /Black TiO ₂	220 W Xe lamp US cleaner	RhB degradation	DE = 98.43% (60 min)	PC: DE = 54.23% (60 min)	[149]
Bi ₂ WO ₆ /g-C ₃ N ₄ /ZnO	300 W Xe lamp 40 kHz US cleaner	RhB degradation	$k = 0.231 \text{ min}^{-1}$	PC: $k = 0.097 \text{ min}^{-1}$	[150]
g-C ₃ N ₄ /Ag/ZnO	50 W LED US cleaner	RhB degradation	DE = 89% (180 min)	PC: DE = 70%	[151]

Table 2. Cont.

Material	Condition	Application	Activity	Blank Control	Ref.
PAN/TiO ₂	350 W Xe lamp 100 kHz EPR spectrometer	RhB degradation	$k = 0.036 \text{ min}^{-1}$	PC: $k = 0.015 \text{ min}^{-1}$	[152]
PbTiO ₃ /g-C ₃ N ₄	300 W Xe lamp ($\lambda > 420 \text{ nm}$) US vibration	RhB degradation	$k = 0.1357 \text{ min}^{-1}$	PC: $k = 0.1044 \text{ min}^{-1}$	[153]
Ag ₂ O/Bi ₄ Ti ₃ O ₁₂	400 W metal halide lamp US vibration	RhB degradation	$k = 0.1557 \text{ min}^{-1}$	PC: $k = 0.0363 \text{ min}^{-1}$	[154]
BaTiO ₃ /SrTiO ₃	LED UV lamp (30 W, 365 nm) 40 kHz US cleaner	RhB degradation	DE = 97.4% (30 min)	SrTiO ₃ : DE = 44.3%	[155]
AgI/ZnO	250 W Xe lamp ($\lambda > 400 \text{ nm}$) US vibration	RhB degradation	$k = 0.037 \text{ min}^{-1}$	ZnO: $k = 0.002 \text{ min}^{-1}$	[156]
Bi ₂ WO ₆	9 W LED 120 W US cleaner	RhB degradation	$k = 0.141 \text{ min}^{-1}$	PC: $k = 0.008 \text{ min}^{-1}$	[157]
Ag/BaTiO ₃	500 W Xe lamp 150 W US vibration	RhB degradation	DE = 70% (120 min)	PC: DE = 25%	[158]
NaNbO ₃ /CuBi ₂ O ₄	50 W LED 35 W US vibration	RhB degradation	DE = 75% (90 min)	NaNbO ₃ : DE = 40%	[159]
BaTiO ₃ /TiO ₂	250 W Xe lamp 40 kHz US cleaner	RhB degradation	$k = 0.0967 \text{ min}^{-1}$	TiO ₂ : $k = 0.0275 \text{ min}^{-1}$	[160]
ZnO@PVDF	300 W Xe lamp magnetic stirrer	RhB degradation	DE \approx 95% (100 min)	PC: DE \approx 55%	[161]
ZnO/ZnS	300 W Xe lamp 180 W US vibration	MB degradation	DE = 53.8% (50 min)	PC: DE = 19.1%	[162]
PMN-PT@SnO ₂	250 W metal halide lamp 45 kHz US cleaner	MB degradation	DE = 97% (120 min)	SnO ₂ : DE = 87%	[163]
Ag ₂ MoO ₄	300 W Xe lamp 40 kHz US vibration	MB degradation	DE = 96.2% (40 min)	PC: DE = 82%	[164]
Ag ₃ PO ₄ /ZnO	300 W Xe lamp ($\lambda > 420 \text{ nm}$) 40 kHz US cleaner	MB degradation	DE = 98.16% (30 min)	PC: DE = 90.18%	[165]
ZnO/ZnS/MoS ₂	300 W Xe lamp magnetic stirrer (1000 rpm)	MB degradation	$k = 0.0411 \text{ min}^{-1}$	PC: $k = 0.0089 \text{ min}^{-1}$	[166]
BaTiO ₃ /CuO	200 W Xe lamp US cleaner	MO degradation	$k = 0.05 \text{ min}^{-1}$	PZC: $k = 0.007 \text{ min}^{-1}$	[167]
BiOBr/BaTiO ₃	Xe lamp (100 mW cm ⁻²) 40 kHz US vibration	MO degradation	$k = 0.1123 \text{ min}^{-1}$	BaTiO ₃ : $k = 0.001 \text{ min}^{-1}$	[168]
ZnO NR/PVDF-HFP	Xe lamp (180 mW/cm ²) magnetic stirrer (1000 rpm)	MO degradation	$k = 0.0399 \text{ min}^{-1}$	PC(200 rpm): $k = 0.0101 \text{ min}^{-1}$	[169]

Table 2. Cont.

Material	Condition	Application	Activity	Blank Control	Ref.
ZnO/MoS ₂	300 W Xe lamp magnetic stirrer (1000 rpm)	MO degradation	DE = 92.7% (50 min)	PC: DE = 50.6%	[170]
TiO ₂ @rGO-F/PVDF-HFP	300 W Xe lamp (UV light) magnetic stirrer	MO degradation	DE = 99% (100 min)	-	[171]
Bi ₂ MoO ₆ /BiOBr	400 W metal halide lamp US cleaner	MV degradation	k = 0.0284 min ⁻¹	Bi ₂ MoO ₆ : k = 0.0082 min ⁻¹	[172]
SrBi ₄ Ti ₄ O ₁₅	300 W Xe lamp 40 kHz US cleaner	TC degradation	k = 0.058 min ⁻¹	PC: k = 0.004 min ⁻¹	[173]
Ti ₃₂ -oxo-cluster/BaTiO ₃ /CuS	300 W Xe lamp 120 W US vibration	TC degradation	DE = 100% (60 min)	PC: DE = 55.67%	[174]
CsCdBO ₃	300 W Xe lamp (λ > 420 nm) 40 kHz US cleaner	TC degradation	DE = 92% (30 min)	-	[175]
ZnO/CdS	300 W Xe lamp 150 W US cleaner	BPA degradation	k = 0.1557 min ⁻¹	PC: k = 0.0135 min ⁻¹	[176]
BiOI/ZnO	300 W Xe lamp 40 kHz US cleaner	BPA degradation	DE = 100% (30 min)	PC: DE = 25%	[177]
PZT/TiO ₂	LED light (15 mW/cm ²) magnetic stirrer (800 rpm)	BPA degradation	DE ≈ 90% (40 min)	PC(200 rpm): DE ≈ 70%	[178]
Au-BiOBr	300 W Xe lamp 40 kHz US cleaner	CBZ degradation	k = 0.091 min ⁻¹	k = 0.00516 min ⁻¹	[179]
BaTiO ₃ /La ₂ Ti ₂ O ₇	300 W Xe lamp (λ > 420 nm) 40 kHz US cleaner	CIP degradation	k = 0.0844 min ⁻¹	BaTiO ₃ : k = 0.0469 min ⁻¹	[180]
ZnS/ Bi ₂ S ₃ -PVDF	300 W Xe lamp (λ > 420 nm) US cleaner	H ₂ production	10.07 mmol g ⁻¹ h ⁻¹	ZnS/Bi ₂ S ₃ : 1.77 mmol g ⁻¹ h ⁻¹	[181]
OH-modified SrTiO ₃	300 W Xe lamp 40 kHz US cleaner	H ₂ production	701.2 μmol g ⁻¹ h ⁻¹	PC: 295.4 μmol g ⁻¹ h ⁻¹	[182]
PbTiO ₃ /CdS	300 W Xe lamp US vibration	H ₂ production	849 μmol g ⁻¹ h ⁻¹	PC: 98.9 μmol g ⁻¹ h ⁻¹	[183]
g-C ₃ N ₄	300 W Xe lamp (λ > 420 nm) US cleaner	H ₂ production	12.16 mmol g ⁻¹ h ⁻¹	PZC: 8.35 mmol g ⁻¹ h ⁻¹	[184]
g-C ₃ N ₄ /LiNbO ₃ /PVDF	300 W Xe lamp magnetic stirrer	H ₂ production	136.02 μmol g ⁻¹ h ⁻¹	PC: 87.71 μmol g ⁻¹ h ⁻¹	[185]
g-C ₃ N ₄ /PDI-g-C ₃ N ₄	300 W Xe lamp 40 kHz US cleaner	H ₂ O ₂ production	625.54 μmol g ⁻¹ h ⁻¹	PC: 149.85 μmol g ⁻¹ h ⁻¹	[186]
ZnS/In ₂ S ₃ /BaTiO ₃	300 W Xe lamp (λ > 400 nm) 40 kHz US horn	H ₂ O ₂ production	228 μmol g ⁻¹ h ⁻¹	72 μmol g ⁻¹ h ⁻¹	[187]

US: ultrasonic; PC: photocatalysis; PZC: piezocatalysis; DE: degradation efficiency; k: degradation rate constant; MB: methylene blue; RhB: rhodamine B; MO: methyl orange; MV: methyl violet; TC: tetracycline; BPA: bisphenol A; CBZ: carbamazepine; CIP: ciprofloxacin.

3.1. The Primary Source of Mechanical Energy

3.1.1. Ultrasound

Ultrasound is currently the most important source of mechanical energy in mechanical-coupled photocatalysis [19,20,188–191]. The photocatalytic reaction is carried out in a custom-made glass vessel exposed to the light and equipped with an ultrasonic generator machine. Ultrasonic waves will produce a cavitation effect in a liquid medium, which can generate microbubbles with a series of dynamic processes, such as contraction, expansion, oscillation, and implosion. After the microbubbles burst, the resulting local hot spot temperature can reach 5000 K, and the pressure can reach 500 atm. Therefore, as for MCP, the ultrasound is always coupled with a cooling system to remove the temperature effect caused by ultrasonic waves [192].

Zeng et al. studied the piezoelectric photocatalytic properties of Au-modified BiOBr, and the reaction setup is shown in Figure 15 [179]. Under the action of ultrasound, the removal rate of carbamazepine (CBZ) reached 95.8% within 30 min, and its rate constant was 1.73 times higher than the sum of the individual piezoelectric and photocatalytic properties. Zhai et al. synthesized BiOX/BaTiO₃ (X = Cl, Br, Cl_{0.166}Br_{0.834}) composites for MO degradation [168]. Under the assistance of ultrasound, the piezoelectric photocatalytic performance ($k = 0.15824 \text{ min}^{-1}$) of the material far exceeds the sum of photocatalysis alone ($k = 0.01159 \text{ min}^{-1}$) and piezoelectric catalysis ($k = 0.01208 \text{ min}^{-1}$). This can be attributed to the synergistic effect of its chemical potential difference and piezoelectric potential difference to stop the recombination of photogenerated carriers. Wang et al. prepared oxygen vacancies (OVs)-dominated SrBi₄Ti₄O₁₅ nanosheets for tetracycline degradation [173]. Under the synergistic effect of visible light and ultrasound, the degradation efficiency was greatly improved, and the oxidation rate constant reached 0.058 min^{-1} , which was 2.15 times and 14.5 times higher than those under only visible light irradiation and only ultrasound, respectively. Xue et al. synthesized a core/shell BaTiO₃/TiO₂ nanocomposite [160]. Under the co-excitation of ultrasound and UV irradiation, the oxidation rate constant of BaTiO₃/TiO₂ nanofibers in RhB dye can reach 0.0967 min^{-1} , which is 3.22 times higher than that under UV irradiation alone.

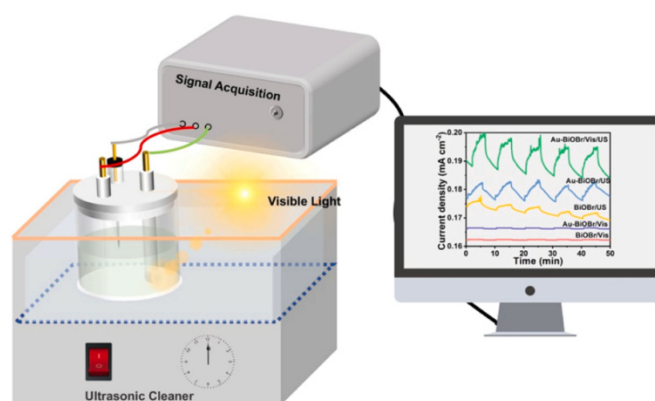


Figure 15. Schematic of the piezo-photocatalytic reactor setup (Reprinted/adapted with permission from Ref. [179]. Copyright 2022, copyright Elsevier).

3.1.2. Stir

The actuation of most piezoelectric materials requires an ultrasound, which undoubtedly greatly limits their applications. Therefore, researchers began to look for simpler driving methods, such as stirring. A new material design was proposed by Zhang et al. By combining semiconductors with a self-driven energy pad, they achieved piezo-photocatalysis under mild mechanical perturbation (stirring) without external energy input [171]. As shown in Figure 16, the energy pad consists of a porous composite graphene-piezoelectric polymer film that combines piezoelectric and dielectric power generation and stores electricity in situ. This energy buffering results in a large and prolonged electric field in

response to mild mechanical perturbations. The experimental results show that the electric field enhances the photocatalytic performance of TiO_2 , BiOI , and CdS by 300%, 21%, and 400%, respectively. Bian et al. prepared core-shell lead zirconate titanate (PZT)/ TiO_2 catalysts [178]. By harvesting the mechanical energy of the water, an internal piezoelectric field is induced. Under stirring at 800 rpm, the transient photocurrent of this catalyst was approximately 1.7 times that at 400 rpm. The experimental results show that the photocatalytic degradation rates of RhB, bisphenol A and phenol are greatly improved. This indicates the facilitation of the stirring-induced piezoelectric field. Xue et al. synthesized ZnO/MoS_2 nanoarrays on Ni foam [170]. The porous structure of the Ni substrate can effectively induce the applied deformation on the nanorod array and generate a built-in piezoelectric field by stirring the water flow, thereby enhancing the photocatalytic performance. Under illumination, the degradation rate of MO increased with the increase of stirring speed, and its highest degradation efficiency reached 92.7%. Fu et al. synthesized ternary $\text{ZnO}/\text{ZnS}/\text{MoS}_2$ nanocomposites and realized piezoelectric photocatalytic performance [166]. Under illumination, the photocatalytic degradation efficiency of the catalyst for MB was 36.15%, and under the combined action of stirring and illumination, the degradation efficiency was increased to 87.14%. This excellent catalytic performance can be attributed to the stirring-induced piezoelectric field, which enhances charge separation.

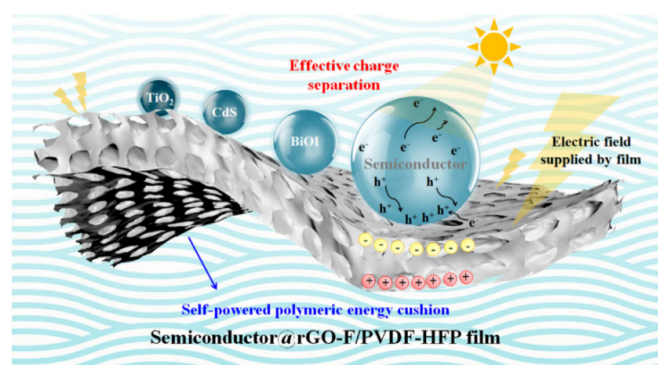


Figure 16. Schematic illustration of the design concept of the hybrid piezophotocatalyst (Reprinted/adapted with permission from Ref. [171]. Copyright 2018, copyright Elsevier).

3.2. Materials for Mechanical-Coupled Photocatalysis

3.2.1. Titanate-Based Materials

Titanate-based materials are widely used in mechanical-coupled photocatalysis, such as BaTiO_3 [147,168,174,180,193–195], SrTiO_3 [155,182,196], and PbTiO_3 [153,183]. Wang et al. synthesized $\text{Ag}_2\text{O}-\text{BaTiO}_3$ hybrid photocatalysts [193]. Under periodic ultrasonic excitation, the spontaneous polarization potential of BaTiO_3 nanocrystals to ultrasonic waves can be used as an alternating built-in electric field to continuously separate photo-induced carriers, which significantly improves the photocatalytic activity and cycling performance of the $\text{Ag}_2\text{O}-\text{BaTiO}_3$ hybrid structure. Li et al. prepared a cyclic Ti_{32} -oxo cluster (CTOC)/ $\text{BaTiO}_3/\text{CuS}$ three-layer heterojunction material for tetracycline degradation [174]. As shown in Figure 17, under the combined action of visible light irradiation and ultrasonic vibration, the catalyst reached 100% decomposition efficiency within 60 min. Under ultrasonic vibration, BaTiO_3 generates a polarized electric field, which inhibits the recombination of photogenerated carriers and improves photocatalytic performance. Zhang et al. synthesized a $\text{BaTiO}_3/\text{SrTiO}_3$ nanocomposite [155]. The degradation rate of $\text{BaTiO}_3/\text{SrTiO}_3$ nanofibers to RhB within 30 min under the combined action of ultrasound and ultraviolet rays was 97.4%, which was 2.2 times that of pure SrTiO_3 nanofibers. Cao et al. synthesized OH-modified SrTiO_3 and used it as a catalyst for piezoelectric photocatalytic H_2 production [182]. Because the catalyst has super-hydrophilic molecular contacts, as well as more oxygen vacancies, the carrier separation is effectively promoted. Under the action of ultrasound, the optimal piezoelectric-photocatalytic H_2 evolution rate

($701.2 \mu\text{mol g}^{-1} \text{h}^{-1}$) was 5.3 times that of the ordinary SrTiO_3 photocatalytic H_2 evolution rate. Jiang et al. studied the piezoelectric effect on the heterogeneous photocatalytic H_2 production of SrTiO_3 (STO) [196]. The piezoelectric effect led by the ultrasonic cavitation had a different influence on heterogeneous photocatalytic H_2 production with or without sacrificial agents. The sacrificial agents with different viscosity and positions of the ultrasonic vibrators also affected the photocatalytic H_2 production of STO. Through in situ photocatalysis and sonophotocatalysis deposition of Pt nanoparticles, it was found that Pt nanoparticles preferred to aggregate on the local surface of STO nanoparticles by ultrasonic cavitation. It was explained that a piezoelectric potential on the local surface of STO would be built by ultrasonic cavitation. Xu et al. combined PbTiO_3 with $\text{g-C}_3\text{N}_4$ to construct a $\text{PbTiO}_3/\text{g-C}_3\text{N}_4$ heterostructured photocatalyst with close contact [153]. By applying ultrasonic-induced mechanical waves, its built-in piezoelectric field was enhanced, which significantly facilitated charge separation. Under ultrasonic conditions, its photocatalytic performance was enhanced by 30%.

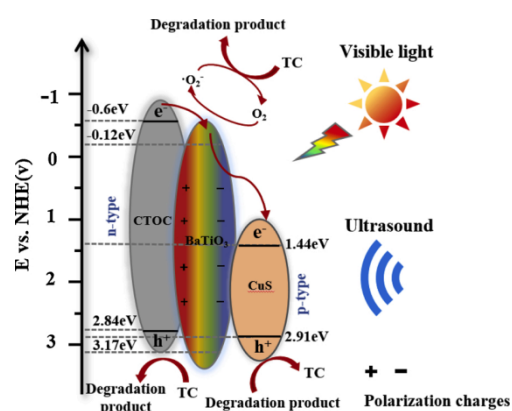


Figure 17. Mechanism for the photo/piezo-catalysis process of CTOC/ BaTiO_3 / CuS composites under visible-light irradiation (Reprinted/adapted with permission from Ref. [174]. Copyright 2021, copyright Elsevier).

3.2.2. Sulfide-Based Materials

In mechanical-coupled photocatalysis, sulfide materials, such as CdS [176,183,197,198], MoS_2 [158,174,175], and ZnS [162,187], have also received much attention. Liu et al. synthesized a novel $\text{PbTiO}_3/\text{CdS}$ hybrid material for photocatalytic H_2 production [183]. The piezo-photocatalysis activity of $\text{PbTiO}_3/\text{CdS}$ ($849.0 \mu\text{mol g}^{-1} \text{h}^{-1}$) was much higher than that of the photocatalysis alone ($98.9 \mu\text{mol g}^{-1} \text{h}^{-1}$), after the alternating piezoelectric potential was introduced by ultrasonic waves. Specifically, as shown in Figure 18, when the direction of the applied periodic force is changed, the direction of the chemical potential difference is also changed and superimposed on the built-in piezoelectric field, thereby accelerating the carrier separation. Zhao et al. prepared CdS nanoparticles with a phase junction by controlling the hydrothermal temperature [197]. Under ultrasonic vibration, a dynamic piezoelectric field is excited inside the CdS nanoparticles. The presence of the piezoelectric field eliminates the shielding effect of carriers in the built-in electric field of the phase junction, enabling the continuous separation of photogenerated carriers, and thereby enhancing the photocatalytic efficiency of CdS . Cui et al. synthesized a $\text{MoS}_2@\text{Ag}_2\text{O}$ heterostructured photocatalyst for efficient all-solar photocatalysis [199]. Under full sunlight and ultrasonic excitation, its MO degradation rate exceeds 95%. During this process, the spontaneous polarization potential of MoS_2 forms a built-in electric field, and the ultrasonic wave as the driving force can continuously change the potential generated by the piezoelectric effect. Therefore, under ultrasonic excitation, the piezoelectric effect enhances the carrier separation, thereby enhancing the photocatalytic performance. Lin et al. developed a monolayer and few-layer MoS_2 nanosheets (NSs) for bacterial inactivation [200]. After 60 min of mechanical vibration or visible light irradiation, MoS_2 NSs can reduce *Escherichia coli* (*E.*

coli) by 99.999%. After the deposition of Au nanoparticles (NPs) on MoS₂ NSs, the time was shortened to 45 min. Furthermore, after synergizing mechanical vibration and near-infrared (NIR) light irradiation, Au-MoS₂ eliminated *E. coli* in only 15 min. Zhai et al. modified In₂S₃ nanosheets with ZnS and BaTiO₃ (ZnS/In₂S₃/BTO) [187]. Under the combined action of visible light and ultrasound, H₂O₂ of approximately 378 μmol g⁻¹ h⁻¹ was generated in 100 min. The enhanced H₂O₂ yield on ZnS/In₂S₃/BTO under piezophotocatalysis can be attributed to the piezoelectric field promoted the separation of photogenerated carriers.

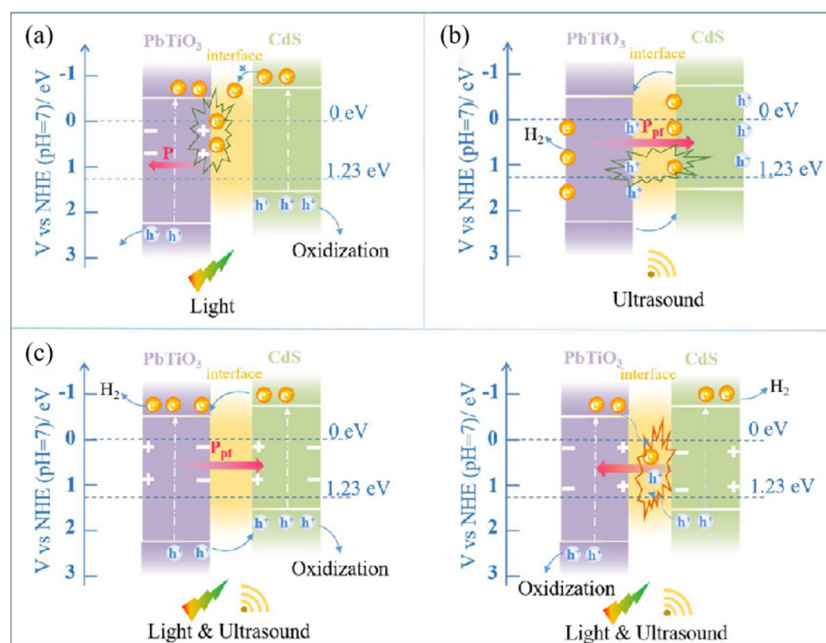


Figure 18. Schematic diagram of (a) photocatalysis, (b) piezocatalysis, and (c) piezo-photocatalysis for PbTiO₃/CdS composites (Reprinted/adapted with permission from Ref. [183]. Copyright 2021, copyright Elsevier).

3.2.3. Polyvinylidene Fluoride

As a common piezoelectric material, polyvinylidene fluoride (PVDF) has great application potential in mechanical-coupled photocatalysis [161,169,171,181,185,201,202]. Sun et al. successfully synthesized a ZnS/Bi₂S₃-PVDF thin film photocatalyst containing S vacancies (ZnS-VS/Bi₂S₃-PVDF) [181]. As shown in Figure 19, the synergistic effect of the PVDF polarization electric field induced by ultrasonic cavitation and the built-in electric field formed between the ZnS-VS/Bi₂S₃ dissimilar junction structure is beneficial to suppressing the recombination of carriers. Its H₂ evolution rate reaches 10.07 mmol g⁻¹ h⁻¹. Zhang et al. prepared a PVDF/MoS₂ cavity/Au heterostructured photocatalyst for MB degradation [202]. The synergistic effect of the MoS₂ cavity and PVDF fibers not only enhances the intrinsic piezoelectric activity of PVDF but also increases the catalytically active centers and free carrier density. The degradation efficiency was as high as 99.9% within 45 min. Lu et al. combined ZnO with PVDF thin films to obtain a bi-piezoelectric integration effect, resulting in enhanced photocatalytic performance [161]. In addition, the piezoelectric potential and photocatalytic activity of the as-prepared ZnO nanorods increased with the increase of the (100) crystal face ratio. Under flowing water conditions, its optimal photocatalytic activity is 10 times that of a single photocatalytic activity. Wang et al. synthesized a bi-piezoelectric ZnO nanorod (NR)/PVDF-HFP sponge-like film [169]. Under water flow, the catalyst can generate an integrated piezoelectric field that greatly drives the separation of photogenerated charge carriers. The results showed that the reaction rate constant for the degradation of MO increased three-fold when the flow rate was increased from 200 rpm to 1000 rpm.

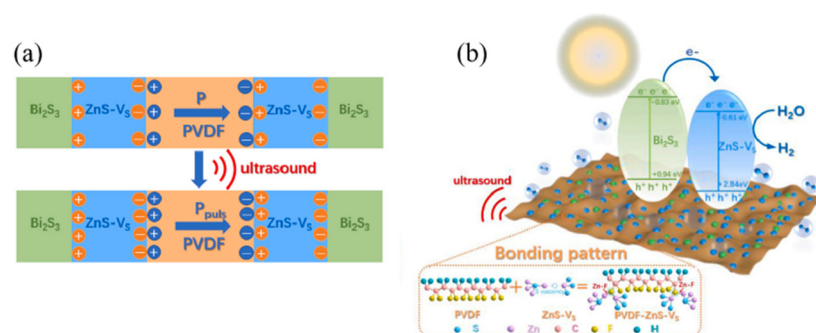


Figure 19. (a) Polarization schematic diagram of PVDF under ultrasonic conditions. (b) Schematic diagram of the photocatalytic mechanism of ZnS-Vs/Bi₂S₃-PVDF under visible light irradiation (Reprinted/adapted with permission from Ref. [181]. Copyright 2022, copyright Elsevier).

4. Electromagnetism-Coupled Photocatalysis (ECP)

The electromagnetism-coupled photocatalysis is divided into two parts to review. They are electro-coupled photocatalysis and magnetism-coupled photocatalysis, respectively. In addition, Table 3 summarizes the application results of electromagnetism-coupled photocatalysis in recent years.

Table 3. Summary of electromagnetism-coupled photocatalysis in recent years.

Material	Condition	Application	Activity	Blank Control	Ref.
ZnO	UV light magnet (600 mT)	MB degradation	DE = 60% (3 min)	PC: DE = 24%	[203]
CoFe ₂ O ₄	UV light (100 mW/cm ²) magnet (200 mT)	MB degradation	DE = 80% (60 min)	PC: DE = 28%	[204]
n-TiO ₂ /PS	400 W UV light power supply (3 V)	MB degradation	DE = 38% (30 min)	PC: DE = 20%	[205]
rGO/TiO ₂	40 W UV lamp Nd ₂ Fe ₁₄ B magnet	MO degradation	DE = 91% (120 min)	TiO ₂ : DE = 68%	[206]
TiO ₂	4 W mercury lamp magnet (280 mT)	MO degradation	DE ≈ 94% (75 min)	PC: DE ≈ 70%	[207]
α-Fe ₂ O ₃ /TiO ₂	Diode Green Laser magnet (400 mT)	RhB degradation	DE ≈ 70% (60 min)	PC: DE ≈ 45%	[208]
Ti _{0.936} O ₂	300 W Xe lamp electromagnet (80 mT)	RhB degradation	k ≈ 0.075 min ⁻¹	PC: k ≈ 0.05 min ⁻¹	[209]
BiFeO ₃	500 W Xe lamp (λ > 420 nm) electrical poling	RhB degradation	k = 0.035 min ⁻¹	PC: k = 0.016 min ⁻¹	[210]
α-Fe ₂ O ₃ /rGO	300 W Xe lamp magnet	CR degradation	DE = 87% (30 min)	PC: DE = 60%	[211]
CoFe ₂ O ₄ /MoS ₂	300 W Xe lamp electromagnet (150 mT)	CR degradation	DE = 96.6% (60 min)	PC(50 mT): DE = 82%	[212]
BiOBr/BNQDs	300 W Xe lamp (λ > 420 nm) magnet	TC degradation	DE = 81% (60 min)	BiOBr: DE = 60%	[213]
hierarchical TiO ₂ microspheres	500 W Xe lamp power supply (2 V)	TBT degradation	k = 0.0488 min ⁻¹	PC: k = 0.0052 min ⁻¹	[214]

Table 3. Cont.

Material	Condition	Application	Activity	Blank Control	Ref.
Mn ₃ O ₄ /γ-MnOOH	300 W Xe lamp magnet (60 mT)	NOR degradation	DE = 98.8% (160 min)	PC: DE = 90.3%	[215]
α-Fe ₂ O ₃ /Zn _{1-x} Fe _x O	Xe lamp (λ > 420 nm) ten magnets (20 mT)	RIB degradation	k = 0.0125 min ⁻¹	PC: k = 0.0072 min ⁻¹	[216]
Au/Fe ₃ O ₄ /N-TiO ₂	70 W tungsten light magnet (180 mT)	H ₂ production	21230 μmol g ⁻¹ h ⁻¹	PC: 7600 μmol g ⁻¹ h ⁻¹	[217]
CdS/MoS ₂ /Mo	300 W Xe lamp (100 mW/cm ²) rotating magnet	H ₂ production	1.97 mmol g ⁻¹ h ⁻¹	PC: 1.04 mmol g ⁻¹ h ⁻¹	[218]
Au-CdS	300 W Xe lamp rotating magnet	H ₂ production	105 μmol g ⁻¹ h ⁻¹	PC: 223 μmol g ⁻¹ h ⁻¹	[219]
Pt/TiO ₂	3 W LED lamp DC power (1 V)	H ₂ production	3242.6 μmol g ⁻¹ h ⁻¹	PC: 1102.8 μmol g ⁻¹ h ⁻¹	[220]
K _{0.5} Na _{0.5} NbO ₃	300 W Xe lamp corona poling (690 kV/cm)	H ₂ production	470 μmol g ⁻¹ h ⁻¹	PC: 63 μmol g ⁻¹ h ⁻¹	[221]
Rutile TiO ₂ nanograss	sunlight power supply (2 V)	Cr ion removal	143.8 mg/g	-	[222]
Bi ₂ MoO ₆	300 W Xe lamp corona poling (20 kV/cm)	CO ₂ reduction	14.38 μmol g ⁻¹ h ⁻¹ (CO)	PC: 4.08 μmol g ⁻¹ h ⁻¹	[223]
BaTiO ₃	300 W Xe lamp magnet	nitrogen fixation	1.93 mgL ⁻¹ h ⁻¹	PC: 1.35 mgL ⁻¹ h ⁻¹	[224]

PC: photocatalysis; DE: degradation efficiency; k: degradation rate constant; MB: methylene blue; RhB: rhodamine B; MO: methyl orange; CR: Congo red; TC: tetracycline; TBT: tributyltin; NOR: norfloxacin; RIB: ribavirin.

4.1. Electro-Coupled Photocatalysis

Adding an external electric field to the photocatalytic system can effectively promote the separation and migration of photogenerated carriers. At present, there are two main ways for researchers to add an electric field: one is to directly connect to an external power source during the photocatalytic process, and the other is to polarize the catalyst in the electric field and then perform photocatalytic experiments.

Directly adding an external electric field during the photocatalytic process is a common utilization method in electro-coupled photocatalysis. Li et al. synthesized rutile TiO₂ nanograss on titanium mesh [222]. By connecting the titanium mesh to a power source, the photocatalytic removal capacity of rutile TiO₂ nanograss for Cr(VI) ions in wastewater can reach 143.8 mg/g under an external electric field and sunlight. Studies have shown that electrons provided by an external electric field can effectively inhibit the recombination of photogenerated carriers, thereby enhancing the catalytic activity. Pan et al. synthesized layered TiO₂ microspheres for the removal of tributyltin (TBT) in electro-coupled photocatalysis, and the reaction setup is shown in Figure 20 [214]. The bias potential provided by the applied electric field greatly facilitates the separation of photogenerated carriers. The results show that the removal reaction rate constant (k = 0.0488 min⁻¹) under electro-coupled photocatalysis is nearly times higher than that under photocatalysis (k = 0.0052 min⁻¹). Zhang et al. developed a new electro-assisted photocatalytic technology for liquid and gas phase reactions (such as water splitting and CO₂ reduction) [220]. They applied a lower external voltage on the self-doped TiO₂ nanotube films. With electrical assistance, the recombination of photogenerated carriers is greatly suppressed, and photoexcited electrons

are ejected from the catalyst, enabling spatial separation of carriers. It is worth mentioning that the photocatalytic redox reaction is integrated on a thin film in this system, rather than taking place on traditional separate electrodes.

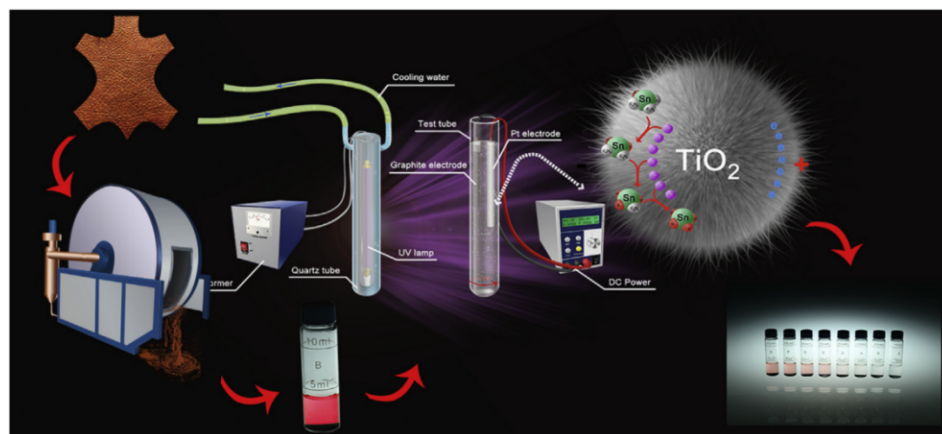


Figure 20. Diagrammatic sketch of the electro-field-assisted-photocatalytic system (Reprinted/adapted with permission from Ref. [214]. Copyright 2017, copyright Elsevier).

In addition to directly adding an external electric field, the researchers also developed another way of electrically coupled photocatalysis. They put the ferroelectric material into an external electric field for polarization before conducting the photocatalytic experiments. The strong ferroelectric field formed by the polarized material can effectively promote charge separation and improve photocatalytic efficiency. Nam et al. prepared polarized $K_{0.5}Na_{0.5}NbO_3$ powder by a corona polarization method for H_2 production [221]. The enlarged positively charged surface of the catalyst promotes the photocatalytic activity. Under optimal conditions, its photocatalytic activity was increased by 7.4 times. Yun et al. prepared well-polarized $BiFeO_3$ nanoparticles by a simple electrical polarization method [210]. The photocatalytic degradation rate of RhB by the polarized $BiFeO_3$ nanoparticles was increased by two times compared with the unpolarized. Its excellent photocatalytic performance can be attributed to the improved carrier separation by ferroelectric polarization. Tian et al. prepared ultrathin Bi_2MoO_6 nanosheets with strong ferroelectricity by a corona polarization method for photocatalytic CO_2 reduction [223]. Its CO generation rate is $14.38 \mu\text{mol g}^{-1} \text{h}^{-1}$, which is more than 10 times higher than that of bulk Bi_2MoO_6 . As shown in Figure 21, this combined strategy significantly promotes the separation of photo-generated electrons and holes, enriches the reaction sites for CO_2 adsorption, and jointly improves the photocatalytic CO_2 reduction performance.

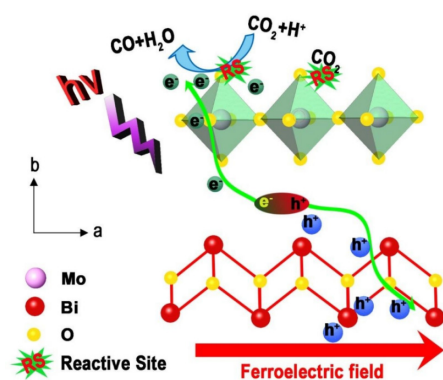


Figure 21. Schematic diagram of ferroelectric field-assisted photocatalysis of Bi_2MoO_6 (Reprinted/adapted with permission from Ref. [223]. Copyright 2020, copyright Royal Society of Chemistry).

4.2. Magnetism-Coupled Photocatalysis

In recent years, more and more attention has been paid to the promotion of magnetic fields on photocatalytic performance. In a magnetism-coupled photocatalytic system, the magnetic-field-induced Lorentz force diverts the charge from its original recombination path, leading to more carriers participating in the reaction, thereby enhancing the photocatalytic activity [206,213,216,225,226]. In addition, for materials with electron spin properties, the magnetic field can also enhance the electron-spin parallel alignment, which also has a positive effect on photocatalytic performance [209,217,227].

Gao et al. reported a Lorentz force-enhanced photogenerated carrier separation strategy using highly crystalline TiO_2 nanosheets with few defects as photocatalysts [225]. Studies have shown that the Lorentz force suppresses photogenerated carrier recombination, making more carriers available for transport in photocatalysts. The results showed that the photocatalytic degradation rate of MO was increased by 26% only by placing permanent magnets under the photocatalytic reactor. Nan et al. synthesized a 3D/2D $\text{Mn}_2\text{O}_3/\text{g-C}_3\text{N}_4$ photocatalyst for simultaneous removal of nitrate and ammonia from polluted water and developed a magnetic field-enhanced photocatalytic system [226]. Under the action of an external magnetic field, the removal efficiencies of nitrate and ammonia were 94.5% and 97.4%, respectively. The external magnetic field promotes the separation of carriers by generating the Lorentz force. Tsang et al. reported a photocatalytic water splitting system based on $\text{Fe}_3\text{O}_4/\text{N-TiO}_2$ magnetic photocatalyst assisted by the local magnetic field effect [217]. As shown in Figure 22, the synergistic effect of the Lorentz force and spin polarization greatly facilitates the charge separation process, thereby enhancing the photocatalytic efficiency. Sang et al. prepared a $\text{CdS}/\text{MoS}_2/\text{Mo}$ hybrid structured photocatalyst and studied the effect of magnetic field on photocatalytic activity [218]. The relative motion between the metal molybdenum sheet and the rotating magnetic field forms a kinematic electromotive force. This electromotive force significantly inhibits the photo-induced carrier recombination of CdS. Under the synergistic effect of MoS_2 co-catalyst, its photocatalytic H_2 production performance is improved by approximately 89% compared with single photocatalysis. Chen et al. synthesized a $\text{Mn}_3\text{O}_4/\gamma\text{-MnOOH}$ photocatalyst for norfloxacin (NOR) degradation [215]. Under the action of magnetic field-assisted visible light, the degradation rate of NOR was 98.8% within 60 min. In neutral media, positively charged NOR and negatively charged catalysts align in the presence of a magnetic field, thereby enhancing the reactivity. Furthermore, the opposing Lorentz force contributed to the mutual attraction between NOR and catalyst, which accelerated NOR degradation.

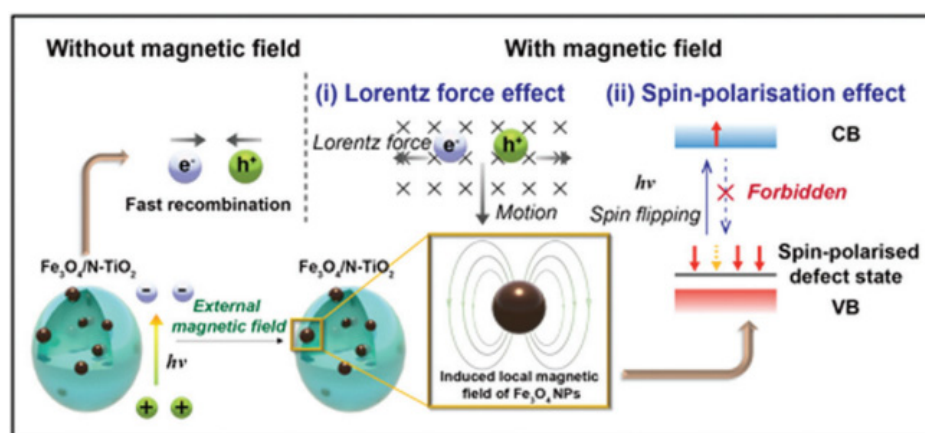


Figure 22. Schematic diagram of magnetic field-promoted photocatalytic water splitting system (Reprinted/adapted with permission from Ref. [217]. Copyright 2022, copyright Royal Society of Chemistry).

5. Conclusions

In this review, we summarized the current research progress of thermal-coupled Photocatalysis (TCP), Mechanical-coupled Photocatalysis (MCP), and Electromagnetism-coupled Photocatalysis (ECP), including the primary sources of external energy, the related materials, and the main applications. These external physical fields can significantly improve the efficiency of the photocatalytic system, which have different mechanisms and respective advantages. In summary, the common feature of these external physical fields coupling to photocatalysis is that external physical fields can re-emit the trapped electrons and drive them rapidly to transfer to the surface of the photocatalyst. Though assisted external physical fields can overcome the inherent weakness of the photocatalytic reaction process, there are still some fundamental issues and challenges to be explored.

- (i) Evaluation of energy conversion efficiency. When external physical fields are applied to the photocatalytic reaction process, additional energy will inevitably be input into the system. Therefore, the solar energy conversion efficiency cannot only be considered when calculating energy conversion efficiency. The extra energy generated by external physical fields should be taken into account.
- (ii) Ubiquitous thermal effect. Thermal energy is low-quality energy. The external physical fields will eventually dissipate into heat energy. The special thermal effects can be generated by microwaves, ultrasonic waves, and electromagnetism waves. Thus, it is important to distinguish thermal effects and non-thermal effects on photocatalysis coupling by external physical fields.
- (iii) A single material response for multiple-physical fields. To realize photocatalysis coupling by external physical fields, composite materials combining photocatalysts and external field absorption materials are usually used. However, the composite materials are complicated both in the synthesis and photocatalytic reaction process. So, it is interesting to explore a single material that can respond to multiple-physical fields. For example, the spontaneous symmetry-breaking semiconductors can absorb multiple-physical fields at the same time, which might be used in photocatalysis coupling by external physical fields.
- (iv) Mechanisms for potential barrier formation by external physical fields. When external physical fields are applied to photocatalysts, a built-in electric field with different directions will be generated to separate the photogenerated carriers. However, mechanisms for potential barrier formation by external physical fields need to be uncovered. Thus, this built-in electric field can be controlled and optimized in favor of photocatalysis coupling by external physical fields.
- (v) Reactor design for photocatalysis coupling by external physical fields. The traditional photocatalytic reactor is not satisfied with photocatalysis coupling by external physical fields. The design principles of the reactor must be high-efficiency and well-adapted for different external physical fields.
- (vi) Horizontal comparison is neglected in the study of photocatalysis coupling by external physical fields. Different external physical fields should make different contributions to photocatalysis. Keeping a balance between photocatalytic efficiency and economic efficiency, the best assisted physical field for photocatalysis needs to be further studied.

Author Contributions: Conceptualization, W.F. and W.S.; writing—original draft preparation, Y.M., Y.Y. and Y.J.; writing—review and editing, W.F. and Y.L. All authors have read and agreed to the published version of the manuscript.

Funding: This research was funded by the National Key Basic Research and Development Program (2018YFB1502001), the National Natural Science Foundation of China (21773153), and the Postgraduate Research & Practice Innovation Program of Jiangsu Province (Yangzhou University, SJCX21_1576).

Conflicts of Interest: The authors declare no conflict of interest.

References

1. Gong, E.; Ali, S.; Hiragond, C.B.; Kim, H.S.; Powar, N.S.; Kim, D.; Kim, H.; In, S.-I. Solar fuels: Research and development strategies to accelerate photocatalytic CO₂ conversion into hydrocarbon fuels. *Energ Environ. Sci.* **2022**, *15*, 880–937. [[CrossRef](#)]
2. Din, M.I.; Khalid, R.; Najeeb, J.; Hussain, Z. Fundamentals and photocatalysis of methylene blue dye using various nanocatalytic assemblies- a critical review. *J. Clean Prod.* **2021**, *298*, 126567. [[CrossRef](#)]
3. Hisatomi, T.; Domen, K. Reaction systems for solar hydrogen production via water splitting with particulate semiconductor photocatalysts. *Nat. Catal.* **2019**, *2*, 387–399. [[CrossRef](#)]
4. Wei, Z.; Liu, J.; Shangguan, W. A review on photocatalysis in antibiotic wastewater: Pollutant degradation and hydrogen production. *Chin. J. Catal.* **2020**, *41*, 1440–1450. [[CrossRef](#)]
5. Shafiq, I.; Shafique, S.; Akhter, P.; Abbas, G.; Qurashi, A.; Hussain, M. Efficient catalyst development for deep aerobic photocatalytic oxidative desulfurization: Recent advances, confines, and outlooks. *Catal. Rev.* **2021**, 1–46. [[CrossRef](#)]
6. Shafiq, I.; Hussain, M.; Rashid, R.; Shafique, S.; Akhter, P.; Yang, W.; Ahmed, A.; Nawaz, Z.; Park, Y.-K. Development of hierarchically porous LaVO₄ for efficient visible-light-driven photocatalytic desulfurization of diesel. *Chem. Eng. J.* **2021**, *420*, 130529. [[CrossRef](#)]
7. Mahboob, I.; Shafiq, I.; Shafique, S.; Akhter, P.; Amjad, U.-e.-S.; Hussain, M.; Park, Y.-K. Effect of active species scavengers in photocatalytic desulfurization of hydrocracker diesel using mesoporous Ag₃VO₄. *Chem. Eng. J.* **2022**, *441*, 136063. [[CrossRef](#)]
8. Lei, W.; Suzuki, N.; Terashima, C.; Fujishima, A. Hydrogel photocatalysts for efficient energy conversion and environmental treatment. *Front. Energy* **2021**, *15*, 577–595. [[CrossRef](#)]
9. Bedia, J.; Muelas-Ramos, V.; Penas-Garzon, M.; Gomez-Aviles, A.; Rodriguez, J.J.; Bolver, C. A review on the synthesis and characterization of metal organic frameworks for photocatalytic water purification. *Catalysts* **2019**, *9*, 52. [[CrossRef](#)]
10. Chen, Y.L.; Bai, X. A review on quantum dots modified g-C₃N₄-based photocatalysts with improved photocatalytic activity. *Catalysts* **2020**, *10*, 142. [[CrossRef](#)]
11. Kumaravel, V.; Imam, M.D.; Badreldin, A.; Chava, R.K.; Do, J.Y.; Kang, M.; Abdel-Wahab, A. Photocatalytic hydrogen production: Role of sacrificial reagents on the activity of oxide, carbon, and sulfide catalysts. *Catalysts* **2019**, *9*, 276. [[CrossRef](#)]
12. Li, X.; Chen, Y.; Tao, Y.; Shen, L.; Xu, Z.; Bian, Z.; Li, H. Challenges of photocatalysis and their coping strategies. *Chem. Catal.* **2022**, *2*, 1315–1345. [[CrossRef](#)]
13. Yuan, J.; Liu, H.; Wang, S.; Li, X. How to apply metal halide perovskites to photocatalysis: Challenges and development. *Nanoscale* **2021**, *13*, 10281–10304. [[CrossRef](#)] [[PubMed](#)]
14. Wang, H.; Li, X.; Zhao, X.; Li, C.; Song, X.; Zhang, P.; Huo, P.; Li, X. A review on heterogeneous photocatalysis for environmental remediation: From semiconductors to modification strategies. *Chin. J. Catal.* **2022**, *43*, 178–214. [[CrossRef](#)]
15. Chen, S.; Yin, H.; Liu, P.; Wang, Y.; Zhao, H. Stabilisation and Performance Enhancement Strategies for Halide Perovskite Photocatalysts. *Adv. Mater.* **2022**, e2203836. [[CrossRef](#)] [[PubMed](#)]
16. Mai, H.; Chen, D.; Tachibana, Y.; Suzuki, H.; Abe, R.; Caruso, R.A. Developing sustainable, high-performance perovskites in photocatalysis: Design strategies and applications. *Chem. Soc. Rev.* **2021**, *50*, 13692–13729. [[CrossRef](#)]
17. Tasleem, S.; Tahir, M. Current trends in strategies to improve photocatalytic performance of perovskites materials for solar to hydrogen production. *Renew. Sustain. Energy Rev.* **2020**, *132*, 110073. [[CrossRef](#)]
18. Xu, Z.; Zhu, Q.; Xi, X.; Xing, M.; Zhang, J. Z-scheme CdS/WO₃ on a carbon cloth enabling effective hydrogen evolution. *Front. Energy* **2021**, *15*, 678–686. [[CrossRef](#)]
19. Li, X.; Wang, W.; Dong, F.; Zhang, Z.; Han, L.; Luo, X.; Huang, J.; Feng, Z.; Chen, Z.; Jia, G.; et al. Recent Advances in Noncontact External-Field-Assisted Photocatalysis: From Fundamentals to Applications. *ACS Catal.* **2021**, *11*, 4739–4769. [[CrossRef](#)]
20. Hu, C.; Tu, S.; Tian, N.; Ma, T.; Zhang, Y.; Huang, H. Photocatalysis Enhanced by External Fields. *Angew. Chem. Int. Ed.* **2021**, *60*, 16309–16328. [[CrossRef](#)]
21. Sun, M.; Zhao, B.; Chen, F.; Liu, C.; Lu, S.; Yu, Y.; Zhang, B. Thermally-assisted photocatalytic CO₂ reduction to fuels. *Chem. Eng. J.* **2021**, *408*, 127280. [[CrossRef](#)]
22. Song, C.; Wang, Z.; Yin, Z.; Xiao, D.; Ma, D. Principles and applications of photothermal catalysis. *Chem. Catal.* **2022**, *2*, 52–83. [[CrossRef](#)]
23. Lu, Y.; Zhang, H.; Fan, D.; Chen, Z.; Yang, X. Coupling solar-driven photothermal effect into photocatalysis for sustainable water treatment. *J. Hazard. Mater.* **2022**, *423*, 127128. [[CrossRef](#)] [[PubMed](#)]
24. Ma, R.; Sun, J.; Li, D.H.; Wei, J.J. Review of synergistic photo-thermo-catalysis: Mechanisms, materials and applications. *Int. J. Hydrogen Energy.* **2020**, *45*, 30288–30324. [[CrossRef](#)]
25. Wang, Z.J.; Song, H.; Liu, H.; Ye, J. Coupling of Solar Energy and Thermal Energy for Carbon Dioxide Reduction: Status and Prospects. *Angew. Chem. Int. Ed.* **2020**, *59*, 8016–8035. [[CrossRef](#)] [[PubMed](#)]
26. Du, S.; Bian, X.; Zhao, Y.; Shi, R.; Zhang, T. Progress and Prospect of Photothermal Catalysis. *Chem. Res. Chin. Univ.* **2022**, *38*, 723–734. [[CrossRef](#)]
27. Keller, N.; Ivanez, J.; Highfield, J.; Ruppert, A.M. Photo-/thermal synergies in heterogeneous catalysis: Towards low-temperature (solar-driven) processing for sustainable energy and chemicals. *Appl. Catal. B Environ.* **2021**, *296*, 120320. [[CrossRef](#)]
28. Cheng, C.; Wang, J.; Guo, X.; Xing, F.; Huang, C.; Song, M. Thermal-assisted photocatalytic H₂ production over sulfur vacancy-rich Co_{0.85}Se/Mn_{0.3}Cd_{0.7}S nanorods under visible light. *Appl. Surf. Sci.* **2021**, *557*, 149812. [[CrossRef](#)]

29. Hu, S.; Shi, J.; Luo, B.; Ai, C.; Jing, D. Significantly enhanced photothermal catalytic hydrogen evolution over Cu₂O-rGO/TiO₂ composite with full spectrum solar light. *J. Colloid Interface Sci.* **2022**, *608*, 2058–2065. [[CrossRef](#)]
30. Li, P.; Liu, L.; An, W.; Wang, H.; Cui, W. Efficient photothermal catalytic CO₂ reduction to CH₃CH₂OH over Cu₂O/g-C₃N₄ assisted by ionic liquids. *Appl. Surf. Sci.* **2021**, *565*, 150448. [[CrossRef](#)]
31. Du, C.; Yan, B.; Yang, G. Promoting photocatalytic hydrogen evolution by introducing hot islands: SnSe nanoparticles on ZnIn₂S₄ monolayer. *Chem. Eng. J.* **2021**, *404*, 126477. [[CrossRef](#)]
32. Lu, Y.; Li, Y.; Wang, Y.; Zhang, J. Two-photon induced NIR active core-shell structured WO₃/CdS for enhanced solar light photocatalytic performance. *Appl. Catal. B Environ.* **2020**, *272*, 118979. [[CrossRef](#)]
33. Tang, Y.; Zhou, W.; Shang, Q.; Guo, Y.; Hu, H.; Li, Z.; Zhang, Y.; Liu, L.; Wang, H.; Tan, X.; et al. Discerning the mechanism of expedited interfacial electron transformation boosting photocatalytic hydrogen evolution by metallic 1T-WS₂-induced photothermal effect. *Appl. Catal. B Environ.* **2022**, *310*, 121295. [[CrossRef](#)]
34. Zhang, X.; Liu, M.; Kang, Z.; Wang, B.; Wang, B.; Jiang, F.; Wang, X.; Yang, D.-P.; Luque, R. NIR-triggered photocatalytic/photothermal/photodynamic water remediation using eggshell-derived CaCO₃/CuS nanocomposites. *Chem. Eng. J.* **2020**, *388*, 124304. [[CrossRef](#)]
35. Ai, Z.; Yang, P.; Lu, X. Degradation of 4-chlorophenol by a microwave assisted photocatalysis method. *J. Hazard. Mater.* **2005**, *124*, 147–152. [[CrossRef](#)] [[PubMed](#)]
36. Nüchter, M.; Müller, U.; Ondruschka, B.; Tied, A.; Lautenschläger, W. Microwave-Assisted Chemical Reactions. *Chem. Eng. Technol.* **2003**, *26*, 1207–1216. [[CrossRef](#)]
37. Ling, L.; Feng, Y.; Li, H.; Chen, Y.; Wen, J.; Zhu, J.; Bian, Z. Microwave induced surface enhanced pollutant adsorption and photocatalytic degradation on Ag/TiO₂. *Appl. Surf. Sci.* **2019**, *483*, 772–778. [[CrossRef](#)]
38. Wang, X.; Jiang, L.; Li, K.; Wang, J.; Fang, D.; Zhang, Y.; Tian, D.; Zhang, Z.; Dionysiou, D.D. Fabrication of novel Z-scheme SrTiO₃/MnFe₂O₄ system with double-response activity for simultaneous microwave-induced and photocatalytic degradation of tetracycline and mechanism insight. *Chem. Eng. J.* **2020**, *400*, 125981. [[CrossRef](#)]
39. Gayathri, P.V.; Yesodharan, S.; Yesodharan, E.P. Microwave/Persulphate assisted ZnO mediated photocatalysis (MW/PS/UV/ZnO) as an efficient advanced oxidation process for the removal of RhB dye pollutant from water. *J. Environ. Chem. Eng.* **2019**, *7*, 103122. [[CrossRef](#)]
40. Mateo, D.; Cerrillo, J.L.; Durini, S.; Gascon, J. Fundamentals and applications of photo-thermal catalysis. *Chem. Soc. Rev.* **2021**, *50*, 2173–2210. [[CrossRef](#)]
41. Linic, S.; Christopher, P.; Ingram, D.B. Plasmonic-metal nanostructures for efficient conversion of solar to chemical energy. *Nat. Mater.* **2011**, *10*, 911–921. [[CrossRef](#)]
42. Manthiram, K.; Alivisatos, A.P. Tunable localized surface plasmon resonances in tungsten oxide nanocrystals. *J. Am. Chem. Soc.* **2012**, *134*, 3995–3998. [[CrossRef](#)] [[PubMed](#)]
43. Linic, S.; Aslam, U.; Boerigter, C.; Morabito, M. Photochemical transformations on plasmonic metal nanoparticles. *Nat. Mater.* **2015**, *14*, 567–576. [[CrossRef](#)] [[PubMed](#)]
44. Chan, G.H.; Zhao, J.; Hicks, E.M.; Schatz, G.C.; Van Duyne, R.P. Plasmonic Properties of Copper Nanoparticles Fabricated by Nanosphere Lithography. *Nano Lett.* **2007**, *7*, 1947–1952. [[CrossRef](#)]
45. Wang, F.; Li, C.; Chen, H.; Jiang, R.; Sun, L.D.; Li, Q.; Wang, J.; Yu, J.C.; Yan, C.H. Plasmonic harvesting of light energy for Suzuki coupling reactions. *J. Am. Chem. Soc.* **2013**, *135*, 5588–5601. [[CrossRef](#)]
46. Yu, G.; Qian, J.; Zhang, P.; Zhang, B.; Zhang, W.; Yan, W.; Liu, G. Collective excitation of plasmon-coupled Au-nanochain boosts photocatalytic hydrogen evolution of semiconductor. *Nat. Commun.* **2019**, *10*, 4912. [[CrossRef](#)]
47. Jian, C.-c.; Zhang, J.; He, W.; Ma, X. Au-Al intermetallic compounds: A series of more efficient LSPR materials for hot carriers-based applications than noble metal Au. *Nano Energy* **2021**, *82*, 105763. [[CrossRef](#)]
48. Han, B.; Chen, L.; Jin, S.; Guo, S.; Park, J.; Yoo, H.S.; Park, J.H.; Zhao, B.; Jung, Y.M. Modulating Mechanism of the LSPR and SERS in Ag/ITO Film: Carrier Density Effect. *J. Phys. Chem. Lett.* **2021**, *12*, 7612–7618. [[CrossRef](#)]
49. Li, P.; Liu, L.; An, W.; Wang, H.; Guo, H.; Liang, Y.; Cui, W. Ultrathin porous g-C₃N₄ nanosheets modified with AuCu alloy nanoparticles and C-C coupling photothermal catalytic reduction of CO to ethanol. *Appl. Catal. B Environ.* **2020**, *266*, 118618. [[CrossRef](#)]
50. Yang, Y.; Cong, Y.; Lin, X.; Cao, B.; Dong, D.; Liu, K.; Xiao, Y.; Shang, J.; Bao, Y.; Liu, Y.; et al. Dual LSPR of Au/W₁₈O₄₉ heterostructures for upconversion enhancement and application of molecular detection. *J. Mater. Chem. A* **2020**, *8*, 4040–4048. [[CrossRef](#)]
51. Kong, W.; Xing, Z.; Fang, B.; Cui, Y.; Li, Z.; Zhou, W. Plasmon Ag/Na-doped defective graphite carbon nitride/NiFe layered double hydroxides Z-scheme heterojunctions toward optimized photothermal-photocatalytic-Fenton performance. *Appl. Catal. B Environ.* **2022**, *304*, 120969. [[CrossRef](#)]
52. Liao, J.; Xu, Y.; Zhao, Y.; Wang, C.-C.; Ge, C. Ag and Fe₃O₄ Comodified WO_{3-x} Nanocomposites for Catalytic Photothermal Degradation of Pharmaceuticals and Personal Care Products. *ACS Appl. Nano Mater.* **2021**, *4*, 1898–1905. [[CrossRef](#)]
53. Wei, T.; Liu, Y.; Dong, W.; Zhang, Y.; Huang, C.; Sun, Y.; Chen, X.; Dai, N. Surface-dependent localized surface plasmon resonances in CuS nanodisks. *ACS Appl. Mater. Interfaces* **2013**, *5*, 10473–10477. [[CrossRef](#)]
54. Liu, Y.; Liu, M.; Swihart, M.T. Reversible Crystal Phase Interconversion between Covellite CuS and High Chalcocite Cu₂S Nanocrystals. *Chem. Mater.* **2017**, *29*, 4783–4791. [[CrossRef](#)]

55. Gao, H.; Chen, Y.; Li, H.; Zhang, F.; Tian, G. Hierarchical Cu₇S₄-Cu₉S₈ heterostructure hollow cubes for photothermal aerobic oxidation of amines. *Chem. Eng. J.* **2019**, *363*, 247–258. [[CrossRef](#)]
56. Lin, H.; Wang, X.; Yu, L.; Chen, Y.; Shi, J. Two-Dimensional Ultrathin MXene Ceramic Nanosheets for Photothermal Conversion. *Nano Lett.* **2017**, *17*, 384–391. [[CrossRef](#)]
57. Naik, G.V.; Schroeder, J.L.; Ni, X.; Kildishev, A.V.; Sands, T.D.; Boltasseva, A. Titanium nitride as a plasmonic material for visible and near-infrared wavelengths [erratum]. *Opt. Mater. Express* **2013**, *3*, 1658. [[CrossRef](#)]
58. Lou, Z.; Gu, Q.; Liao, Y.; Yu, S.; Xue, C. Promoting Pd-catalyzed Suzuki coupling reactions through near-infrared plasmon excitation of WO_{3-x} nanowires. *Appl. Catal. B Environ.* **2016**, *184*, 258–263. [[CrossRef](#)]
59. Wang, Y.; Liu, M.; Wu, C.; Gao, J.; Li, M.; Xing, Z.; Li, Z.; Zhou, W. Hollow Nanoboxes Cu_{2-x}S@ZnIn₂S₄ Core-Shell S-Scheme Heterojunction with Broad-Spectrum Response and Enhanced Photothermal-Photocatalytic Performance. *Small* **2022**, *18*, e2202544. [[CrossRef](#)]
60. Xie, Z.; Duo, Y.; Lin, Z.; Fan, T.; Xing, C.; Yu, L.; Wang, R.; Qiu, M.; Zhang, Y.; Zhao, Y.; et al. The Rise of 2D Photothermal Materials beyond Graphene for Clean Water Production. *Adv. Sci.* **2020**, *7*, 1902236. [[CrossRef](#)]
61. Wang, J.; Li, Y.; Deng, L.; Wei, N.; Weng, Y.; Dong, S.; Qi, D.; Qiu, J.; Chen, X.; Wu, T. High-Performance Photothermal Conversion of Narrow-Bandgap Ti₂O₃ Nanoparticles. *Adv. Mater.* **2017**, *29*, 1603730. [[CrossRef](#)] [[PubMed](#)]
62. Wang, Z.; Yang, C.; Lin, T.; Yin, H.; Chen, P.; Wan, D.; Xu, F.; Huang, F.; Lin, J.; Xie, X.; et al. Visible-light photocatalytic, solar thermal and photoelectrochemical properties of aluminium-reduced black titania. *Energy Environ. Sci.* **2013**, *6*, 3007–3014. [[CrossRef](#)]
63. Ye, M.; Jia, J.; Wu, Z.; Qian, C.; Chen, R.; O'Brien, P.G.; Sun, W.; Dong, Y.; Ozin, G.A. Synthesis of Black TiO_x Nanoparticles by Mg Reduction of TiO₂ Nanocrystals and their Application for Solar Water Evaporation. *Adv. Energy Mater.* **2017**, *7*, 1601811. [[CrossRef](#)]
64. Low, J.; Zhang, L.; Zhu, B.; Liu, Z.; Yu, J. TiO₂ Photonic Crystals with Localized Surface Photothermal Effect and Enhanced Photocatalytic CO₂ Reduction Activity. *ACS Sustain. Chem. Eng.* **2018**, *6*, 15653–15661. [[CrossRef](#)]
65. Pan, J.; Yu, X.; Dong, J.; Zhao, L.; Liu, L.; Liu, J.; Zhao, X.; Liu, L. Diatom-Inspired TiO₂-PANi-Decorated Bilayer Photothermal Foam for Solar-Driven Clean Water Generation. *ACS Appl. Mater. Interfaces* **2021**, *13*, 58124–58133. [[CrossRef](#)]
66. Chou, S.S.; Kaehr, B.; Kim, J.; Foley, B.M.; De, M.; Hopkins, P.E.; Huang, J.; Brinker, C.J.; Dravid, V.P. Chemically exfoliated MoS₂ as near-infrared photothermal agents. *Angew. Chem. Int. Ed.* **2013**, *52*, 4160–4164. [[CrossRef](#)] [[PubMed](#)]
67. Ghim, D.; Jiang, Q.; Cao, S.; Singamaneni, S.; Jun, Y.-S. Mechanically interlocked 1T/2H phases of MoS₂ nanosheets for solar thermal water purification. *Nano Energy* **2018**, *53*, 949–957. [[CrossRef](#)]
68. Ding, D.; Huang, W.; Song, C.; Yan, M.; Guo, C.; Liu, S. Non-stoichiometric MoO_{3-x} quantum dots as a light-harvesting material for interfacial water evaporation. *Chem. Commun.* **2017**, *53*, 6744–6747. [[CrossRef](#)]
69. Qi, Y.; Song, L.; Ouyang, S.; Liang, X.; Ning, S.; Zhang, Q.; Ye, J. Photoinduced Defect Engineering: Enhanced Photothermal Catalytic Performance of 2D Black In₂O_{3-x} Nanosheets with Bifunctional Oxygen Vacancies. *Adv. Mater.* **2020**, *32*, e1903915. [[CrossRef](#)]
70. Zhang, Y.; Heo, Y.-J.; Son, Y.-R.; In, I.; An, K.-H.; Kim, B.-J.; Park, S.-J. Recent advanced thermal interfacial materials: A review of conducting mechanisms and parameters of carbon materials. *Carbon* **2019**, *142*, 445–460. [[CrossRef](#)]
71. Li, J.; Ma, L.; Fu, C.; Huang, Y.; Luo, B.; Cao, J.; Geng, J.; Jing, D. Urchinlike Carbon-Coated TiO₂ Microspheres with Enhanced Photothermal-Photocatalytic Hydrogen Evolution Performance for Full-Spectrum Solar Energy Conversion. *Ind. Eng. Chem. Res.* **2022**, *61*, 6436–6447. [[CrossRef](#)]
72. Zhang, Q.; Xu, W.; Wang, X. Carbon nanocomposites with high photothermal conversion efficiency. *Sci. China Mater.* **2018**, *61*, 905–914. [[CrossRef](#)]
73. Tong, X.; Li, N.; Zeng, M.; Wang, Q. Organic phase change materials confined in carbon-based materials for thermal properties enhancement: Recent advancement and challenges. *Renew. Sustain. Energy Rev.* **2019**, *108*, 398–422. [[CrossRef](#)]
74. Guo, X.; Cheng, S.; Cai, W.; Zhang, Y.; Zhang, X.-a. A review of carbon-based thermal interface materials: Mechanism, thermal measurements and thermal properties. *Mater. Design* **2021**, *209*, 109936. [[CrossRef](#)]
75. Chen, C.; Li, Y.; Song, J.; Yang, Z.; Kuang, Y.; Hitz, E.; Jia, C.; Gong, A.; Jiang, F.; Zhu, J.Y.; et al. Highly Flexible and Efficient Solar Steam Generation Device. *Adv. Mater.* **2017**, *29*, 1701756. [[CrossRef](#)]
76. Yu, Y.; Chen, S.; Jia, Y.; Qi, T.; Xiao, L.; Cui, X.; Zhuang, D.; Wei, J. Ultra-black and self-cleaning all carbon nanotube hybrid films for efficient water desalination and purification. *Carbon* **2020**, *169*, 134–141. [[CrossRef](#)]
77. Zhang, F.; Xu, D.; Zhang, D.; Ma, L.; Wang, J.; Huang, Y.; Chen, M.; Qian, H.; Li, X. A durable and photothermal superhydrophobic coating with entwined CNTs-SiO₂ hybrids for anti-icing applications. *Chem. Eng. J.* **2021**, *423*, 130238. [[CrossRef](#)]
78. Robinson, J.T.; Tabakman, S.M.; Liang, Y.; Wang, H.; Casalongue, H.S.; Vinh, D.; Dai, H. Ultrasmall reduced graphene oxide with high near-infrared absorbance for photothermal therapy. *J. Am. Chem. Soc.* **2011**, *133*, 6825–6831. [[CrossRef](#)]
79. Wang, Y.; Wang, C.; Song, X.; Megarajan, S.K.; Jiang, H. A facile nanocomposite strategy to fabricate a rGO-MWCNT photothermal layer for efficient water evaporation. *J. Mater. Chem. A* **2018**, *6*, 963–971. [[CrossRef](#)]
80. Zhang, C.-R.; Cui, W.-R.; Niu, C.-P.; Yi, S.-M.; Liang, R.-P.; Qi, J.-X.; Chen, X.-J.; Jiang, W.; Zhang, L.; Qiu, J.-D. rGO-based covalent organic framework hydrogel for synergistically enhance uranium capture capacity through photothermal desalination. *Chem. Eng. J.* **2022**, *428*, 131178. [[CrossRef](#)]

81. Zha, Z.; Yue, X.; Ren, Q.; Dai, Z. Uniform polypyrrole nanoparticles with high photothermal conversion efficiency for photothermal ablation of cancer cells. *Adv. Mater.* **2013**, *25*, 777–782. [[CrossRef](#)]
82. Wu, X.; Jiang, Q.; Ghim, D.; Singamaneni, S.; Jun, Y.-S. Localized heating with a photothermal polydopamine coating facilitates a novel membrane distillation process. *J. Mater. Chem. A* **2018**, *6*, 18799–18807. [[CrossRef](#)]
83. Wang, X.; Liu, Q.; Wu, S.; Xu, B.; Xu, H. Multilayer Polypyrrole Nanosheets with Self-Organized Surface Structures for Flexible and Efficient Solar-Thermal Energy Conversion. *Adv. Mater.* **2019**, *31*, e1807716. [[CrossRef](#)] [[PubMed](#)]
84. Chen, Z.; Luo, Y.; Li, Q.; Chen, X. Microgroove-Structured PDA/PEI/PPy@PI-MS Photothermal Aerogel with a Multilevel Water Transport Network for Highly Salt-Rejecting Solar-Driven Interfacial Evaporation. *ACS Appl. Mater. Interfaces* **2021**, *13*, 40531–40542. [[CrossRef](#)] [[PubMed](#)]
85. Yu, H.; Sun, C.; Xuan, Y.; Zhang, K.; Chang, K. Full solar spectrum driven plasmonic-assisted efficient photocatalytic CO₂ reduction to ethanol. *Chem. Eng. J.* **2022**, *430*, 132940. [[CrossRef](#)]
86. Lu, C.; Li, X.; Li, J.; Mao, L.; Zhu, M.; Chen, Q.; Wen, L.; Li, B.; Guo, T.; Lou, Z. Nonmetallic surface plasmon resonance coupling with pyroelectric effect for enhanced near-infrared-driven CO₂ reduction. *Chem. Eng. J.* **2022**, *445*, 136739. [[CrossRef](#)]
87. Huang, W.; Zhang, L.; Li, Z.; Zhang, X.; Dong, X.; Zhang, Y. Efficient CO₂ reduction with H₂O via photothermal chemical reaction based on Au-MgO dual catalytic site on TiO₂. *J. CO₂ Util.* **2022**, *55*, 101801. [[CrossRef](#)]
88. Han, R.; Chen, L.; Xing, B.; Guo, Q.; Tian, J.; Sha, N.; Zhao, Z. Pr³⁺-doped La_{1-x}Pr_xMn_{0.6}Ni_{0.4}O_{3-δ} as efficient artificial photosynthesis catalysts for solar methanol. *Catal. Commun.* **2022**, *165*, 106440. [[CrossRef](#)]
89. Fiorenza, R.; Bellardita, M.; Balsamo, S.A.; Spitaleri, L.; Gulino, A.; Condorelli, M.; D'Urso, L.; Scirè, S.; Palmisano, L. A solar photothermocatalytic approach for the CO₂ conversion: Investigation of different synergisms on CoO-CuO/brookite TiO₂-CeO₂ catalysts. *Chem. Eng. J.* **2022**, *428*, 131249. [[CrossRef](#)]
90. Bian, H.; Liu, T.; Li, D.; Xu, Z.; Lian, J.; Chen, M.; Yan, J.; Frank Liu, S. Unveiling the effect of interstitial dopants on CO₂ activation over CsPbBr₃ catalyst for efficient photothermal CO₂ reduction. *Chem. Eng. J.* **2022**, *435*, 135071. [[CrossRef](#)]
91. Zheng, Y.; Zhang, L.; Guan, J.; Qian, S.; Zhang, Z.; Ngaw, C.K.; Wan, S.; Wang, S.; Lin, J.; Wang, Y. Controlled Synthesis of Cu⁰/Cu₂O for Efficient Photothermal Catalytic Conversion of CO₂ and H₂O. *Acs Sustain. Chem. Eng.* **2021**, *9*, 1754–1761. [[CrossRef](#)]
92. Wang, Y.; Zhou, Q.; Zhu, Y.; Xu, D. High efficiency reduction of CO₂ to CO and CH₄ via photothermal synergistic catalysis of lead-free perovskite Cs₃Sb₂I₉. *Appl. Catal. B Environ.* **2021**, *294*, 120236. [[CrossRef](#)]
93. Li, Y.; Wen, M.; Wang, Y.; Tian, G.; Wang, C.; Zhao, J. Plasmonic Hot Electrons from Oxygen Vacancies for Infrared Light-Driven Catalytic CO₂ Reduction on Bi₂O_{3-x}. *Angew. Chem. Int. Ed.* **2021**, *60*, 910–916. [[CrossRef](#)] [[PubMed](#)]
94. Wang, H.; Wang, Y.; Guo, L.; Zhang, X.; Ribeiro, C.; He, T. Solar-heating boosted catalytic reduction of CO₂ under full-solar spectrum. *Chin. J. Catal.* **2020**, *41*, 131–139. [[CrossRef](#)]
95. Yu, F.; Wang, C.; Li, Y.; Ma, H.; Wang, R.; Liu, Y.; Suzuki, N.; Terashima, C.; Ohtani, B.; Ochiai, T.; et al. Enhanced Solar Photothermal Catalysis over Solution Plasma Activated TiO₂. *Adv. Sci.* **2020**, *7*, 2000204. [[CrossRef](#)]
96. Yang, F.; Li, Z.; Xie, Y.; Wang, S.; Li, M.; Liao, L.; Zhou, W. Ag/polydopamine nanoparticles co-decorated defective mesoporous carbon nitride nanosheets assemblies for wide spectrum response and robust photothermal-photocatalytic performance. *Appl. Surf. Sci.* **2022**, *598*, 153895. [[CrossRef](#)]
97. Li, B.; Ding, Y.; Li, Q.; Guan, Z.; Zhang, M.; Yang, J. The photothermal effect enhance visible light-driven hydrogen evolution using urchin-like hollow RuO₂/TiO₂/Pt/C nanomaterial. *J. Alloys Compd.* **2022**, *890*, 161722. [[CrossRef](#)]
98. Guo, X.; Li, J.; Wang, Y.; Rui, Z. Photothermocatalytic water splitting over Pt/ZnIn₂S₄ for hydrogen production without external heat. *Catal. Today* **2022**, *402*, 210–219. [[CrossRef](#)]
99. Cheng, X.; Wang, L.; Xie, L.; Sun, C.; Zhao, W.; Liu, X.; Zhuang, Z.; Liu, S.; Zhao, Q. Defect-driven selective oxidation of MoS₂ nanosheets with photothermal effect for Photo-Catalytic hydrogen evolution reaction. *Chem. Eng. J.* **2022**, *439*, 135757. [[CrossRef](#)]
100. Li, Y.; Xue, J.; Shen, Q.; Jia, S.; Li, Q.; Li, Y.; Liu, X.; Jia, H. Construction of a ternary spatial junction in yolk-shell nanoreactor for efficient photo-thermal catalytic hydrogen generation. *Chem. Eng. J.* **2021**, *423*, 130188. [[CrossRef](#)]
101. Li, X.; Zhao, S.; Duan, X.; Zhang, H.; Yang, S.-z.; Zhang, P.; Jiang, S.P.; Liu, S.; Sun, H.; Wang, S. Coupling hydrothermal and photothermal single-atom catalysis toward excellent water splitting to hydrogen. *Appl. Catal. B Environ.* **2021**, *283*, 119660. [[CrossRef](#)]
102. Li, M.; Sun, J.; Chen, G.; Yao, S.; Cong, B.; Liu, P. Construction photothermal/pyroelectric property of hollow FeS₂/Bi₂S₃ nanostructure with enhanced full spectrum photocatalytic activity. *Appl. Catal. B Environ.* **2021**, *298*, 120573. [[CrossRef](#)]
103. Guo, S.; Li, X.; Li, J.; Wei, B. Boosting photocatalytic hydrogen production from water by photothermally induced biphasic systems. *Nat. Commun.* **2021**, *12*, 1343. [[CrossRef](#)] [[PubMed](#)]
104. Ng, S.W.L.; Gao, M.; Lu, W.; Hong, M.; Ho, G.W. Selective Wavelength Enhanced Photochemical and Photothermal H₂ Generation of Classical Oxide Supported Metal Catalyst. *Adv. Funct. Mater.* **2021**, *31*, 2104750. [[CrossRef](#)]
105. Luo, X.; Li, R.; Homewood, K.P.; Chen, X.; Gao, Y. Hybrid 0D/2D Ni₂P quantum dot loaded TiO₂(B) nanosheet photothermal catalysts for enhanced hydrogen evolution. *Appl. Surf. Sci.* **2020**, *505*, 144099. [[CrossRef](#)]
106. Ren, H.; Yang, J.-L.; Yang, W.-M.; Zhong, H.-L.; Lin, J.-S.; Radjenovic, P.M.; Sun, L.; Zhang, H.; Xu, J.; Tian, Z.-Q.; et al. Core-Shell-Satellite Plasmonic Photocatalyst for Broad-Spectrum Photocatalytic Water Splitting. *ACS Mater. Lett.* **2020**, *3*, 69–76. [[CrossRef](#)]

107. Zhang, M.; Hu, Q.; Ma, K.; Ding, Y.; Li, C. Pyroelectric effect in CdS nanorods decorated with a molecular Co-catalyst for hydrogen evolution. *Nano Energy* **2020**, *73*, 104810. [[CrossRef](#)]
108. Dai, B.; Fang, J.; Yu, Y.; Sun, M.; Huang, H.; Lu, C.; Kou, J.; Zhao, Y.; Xu, Z. Construction of Infrared-Light-Responsive Photoinduced Carriers Driver for Enhanced Photocatalytic Hydrogen Evolution. *Adv. Mater.* **2020**, *32*, e1906361. [[CrossRef](#)]
109. Yang, F.; Wang, S.; Li, Z.; Xu, Y.; Yang, W.; Yv, C.; Yang, D.; Xie, Y.; Zhou, W. Polydopamine/defective ultrathin mesoporous graphitic carbon nitride nanosheets as Z-scheme organic assembly for robust photothermal-photocatalytic performance. *J. Colloid Interface Sci.* **2022**, *613*, 775–785. [[CrossRef](#)]
110. Wang, R.; Shan, G.; Wang, T.; Yin, D.; Chen, Y. Photothermal enhanced photocatalytic activity based on Ag-doped CuS nanocomposites. *J. Alloys Compd.* **2021**, *864*, 158591. [[CrossRef](#)]
111. Shi, S.; Han, X.; Liu, J.; Lan, X.; Feng, J.; Li, Y.; Zhang, W.; Wang, J. Photothermal-boosted effect of binary CuFe bimetallic magnetic MOF heterojunction for high-performance photo-Fenton degradation of organic pollutants. *Sci. Total Environ.* **2021**, *795*, 148883. [[CrossRef](#)] [[PubMed](#)]
112. Liu, X.; Wang, W.; Lin, H.; Shen, Y.; Fang, Q.; Liu, F. Construction of hierarchical Prussian blue microcrystal with high sunlight absorption for efficient photo-thermal degradation of organic pollutants. *Sep. Purif. Technol.* **2021**, *269*, 118724. [[CrossRef](#)]
113. Li, Y.; Chang, H.; Wang, Z.; Shen, Q.; Liu, X.; Xue, J.; Jia, H. A 3D C@TiO₂ multishell nanoframe for simultaneous photothermal catalytic hydrogen generation and organic pollutant degradation. *J. Colloid Interface Sci.* **2022**, *609*, 535–546. [[CrossRef](#)]
114. Li, J.; Zhang, J.; Jiao, X.; Shi, J.; Ye, J.; Song, K.; Bao, J.; Li, G.; Lei, K. NIR-driven PtCu-alloy nanocages via photothermal enhanced fenton catalytic degradation of pollutant dyes under neutral pH. *J. Alloys Compd.* **2022**, *895*, 162624. [[CrossRef](#)]
115. Lin, E.; Huang, R.; Wu, J.; Kang, Z.; Ke, K.; Qin, N.; Bao, D. Recyclable CoFe₂O₄ modified BiOCl hierarchical microspheres utilizing photo, photothermal and mechanical energy for organic pollutant degradation. *Nano Energy* **2021**, *89*, 106403. [[CrossRef](#)]
116. Chen, J.; Luo, W.; Yu, S.; Yang, X.; Wu, Z.; Zhang, H.; Gao, J.; Mai, Y.-W.; Li, Y.; Jia, Y. Synergistic effect of photocatalysis and pyrocatalysis of pyroelectric ZnSnO₃ nanoparticles for dye degradation. *Ceram. Int.* **2020**, *46*, 9786–9793. [[CrossRef](#)]
117. Tian, J.; Wu, S.; Liu, S.; Zhang, W. Photothermal enhancement of highly efficient photocatalysis with bioinspired thermal radiation balance characteristics. *Appl. Surf. Sci.* **2022**, *592*, 153304. [[CrossRef](#)]
118. Okeil, S.; Yadav, S.; Bruns, M.; Zintler, A.; Molina-Luna, L.; Schneider, J.J. Photothermal catalytic properties of layered titanium chalcogenide nanomaterials. *Dalton Trans.* **2020**, *49*, 1032–1047. [[CrossRef](#)]
119. Zhu, Q.; Song, J.; Liu, Z.; Wu, K.; Li, X.; Chen, Z.; Pang, H. Photothermal catalytic degradation of textile dyes by laccase immobilized on Fe₃O₄@SiO₂ nanoparticles. *J. Colloid. Interf. Sci.* **2022**, *623*, 992–1001. [[CrossRef](#)]
120. Qi, Y.; Yang, Z.; Jiang, Y.; Han, H.; Wu, T.; Wu, L.; Liu, J.; Wang, Z.; Wang, F. Platinum–Copper Bimetallic Nanoparticles Supported on TiO₂ as Catalysts for Photo–thermal Catalytic Toluene Combustion. *ACS Appl. Nano Mater.* **2022**, *5*, 1845–1854. [[CrossRef](#)]
121. Li, J.; Feng, J.; Guo, X.; Fang, H.; Chen, J.; Ma, C.; Li, R.; Wang, Y.; Rui, Z. Defect-band bridge photothermally activates Type III heterojunction for CO₂ reduction and typical VOCs oxidation. *Appl. Catal. B Environ.* **2022**, *309*, 121248. [[CrossRef](#)]
122. Li, A.; Zhang, Q.; Zhao, S.; Chong, Y.; Wu, P.; Li, Y.; Jin, X.; Chen, G.; Qiu, Y.; Yang, S.; et al. A dual plasmonic core–shell Pt/[TiN@TiO₂] catalyst for enhanced photothermal synergistic catalytic activity of VOCs abatement. *Nano Res.* **2022**, *15*, 7071–7080. [[CrossRef](#)]
123. Xie, A.; Wang, H.; Qi, S.; Li, X.; Zhu, Z.; Zhang, W.; Wang, Q.; Tang, Y.; Luo, S. Mesoporous SmMnO₃/CuMnO catalyst for photothermal synergistic degradation of gaseous toluene. *Ceram. Int.* **2021**, *47*, 31485–31496. [[CrossRef](#)]
124. Li, J.; Zhang, M.; Elimian, E.A.; Lv, X.; Chen, J.; Jia, H. Convergent ambient sunlight-powered multifunctional catalysis for toluene abatement over in situ exsolution of Mn₃O₄ on perovskite parent. *Chem. Eng. J.* **2021**, *412*, 128560. [[CrossRef](#)]
125. Xiao, Y.; Wang, K.; Yang, Z.; Xing, Z.; Li, Z.; Pan, K.; Zhou, W. Plasma Cu-decorated TiO_{2-x}/CoP particle-level hierarchical heterojunctions with enhanced photocatalytic-photothermal performance. *J. Hazard. Mater.* **2021**, *414*, 125487. [[CrossRef](#)]
126. Jiang, H.; Xing, Z.; Zhao, T.; Yang, Z.; Wang, K.; Li, Z.; Yang, S.; Xie, L.; Zhou, W. Plasmon Ag nanoparticle/Bi₂S₃ ultrathin nanobelt/oxygen-doped flower-like MoS₂ nanosphere ternary heterojunctions for promoting charge separation and enhancing solar-driven photothermal and photocatalytic performances. *Appl. Catal. B Environ.* **2020**, *274*, 118947. [[CrossRef](#)]
127. Guo, M.; Zhao, T.; Xing, Z.; Qiu, Y.; Pan, K.; Li, Z.; Yang, S.; Zhou, W. Hollow Octahedral Cu_{2-x}S/CdS/Bi₂S₃ p-n-p Type Tandem Heterojunctions for Efficient Photothermal Effect and Robust Visible-Light-Driven Photocatalytic Performance. *ACS Appl. Mater. Interfaces* **2020**, *12*, 40328–40338. [[CrossRef](#)]
128. Guo, M.; Xing, Z.; Zhao, T.; Qiu, Y.; Tao, B.; Li, Z.; Zhou, W. Hollow flower-like polyhedral α -Fe₂O₃/Defective MoS₂/Ag Z-scheme heterojunctions with enhanced photocatalytic-Fenton performance via surface plasmon resonance and photothermal effects. *Appl. Catal. B Environ.* **2020**, *272*, 118978. [[CrossRef](#)]
129. Lee, H.; Park, S.H.; Park, Y.-K.; Kim, S.-J.; Seo, S.-G.; Ki, S.J.; Jung, S.-C. Photocatalytic reactions of 2,4-dichlorophenoxyacetic acid using a microwave-assisted photocatalysis system. *Chem. Eng. J.* **2015**, *278*, 259–264. [[CrossRef](#)]
130. Li, M.; Xing, Z.; Zhang, Z.; Wang, Y.; Liu, M.; Li, Z.; Wang, N.; Zhou, W. Hollow core-shell Z-scheme heterojunction on self-floating carbon fiber cloth with robust photocatalytic-photothermal performance. *J. Clean. Prod.* **2022**, *360*, 132166. [[CrossRef](#)]
131. Qiu, Y.; Xing, Z.; Guo, M.; Li, Z.; Wang, N.; Zhou, W. Hollow cubic Cu_{2-x}S/Fe-POMs/AgVO₃ dual Z-scheme heterojunctions with wide-spectrum response and enhanced photothermal and photocatalytic-fenton performance. *Appl. Catal. B Environ.* **2021**, *298*, 120628. [[CrossRef](#)]

132. Yuan, Y.; Pan, W.-g.; Guo, R.-t.; Hong, L.-f.; Lin, Z.-d.; Ji, X.-y. Flower spherical-like Bi₇O₉I₃/AgI S-scheme heterojunction for phenol photodegradation: The synergetic effect of dual surface plasmon resonance and photothermal property. *Sep. Purif. Technol.* **2022**, *297*, 121538. [[CrossRef](#)]
133. Wang, Z.; Wang, Y.; Zhang, Y.; Sun, X.; Lou, Y.; Zhang, Y.; Dong, Y.; Pan, C.; Zhu, Y. Efficient photothermal degradation on Bi₁₂CoO₂₀ sillenite with a strong internal electric field induced by the thermal effect. *Appl. Catal. B Environ.* **2022**, *313*, 121452. [[CrossRef](#)]
134. Zheng, Y.; Tan, J.; Zhang, G.; Ma, Y.; Liu, F.; Liu, M.; Wang, Y.; Zou, H.; Huang, H. Yolk-Shell AuAgPt Alloy Nanostructures with Tunable Morphologies: Plasmon-Enhanced Photothermal and Catalytic Properties. *Adv. Energy Sustain. Res.* **2022**, *3*, 2100222. [[CrossRef](#)]
135. Wang, R.; Hao, Q.; Feng, J.; Wang, G.-C.; Ding, H.; Chen, D.; Ni, B. Enhanced separation of photogenerated charge carriers and catalytic properties of ZnO-MnO₂ composites by microwave and photothermal effect. *J. Alloys Compd.* **2019**, *786*, 418–427. [[CrossRef](#)]
136. Borjigin, B.; Ding, L.; Li, H.; Wang, X. A solar light-induced photo-thermal catalytic decontamination of gaseous benzene by using Ag/Ag₃PO₄/CeO₂ heterojunction. *Chem. Eng. J.* **2020**, *402*, 126070. [[CrossRef](#)]
137. Zeng, X.; Shan, C.; Sun, M.; Ding, D.; Rong, S. Graphene enhanced α -MnO₂ for photothermal catalytic decomposition of carcinogen formaldehyde. *Chin. Chem. Lett.* **2022**, *33*, 4771–4775. [[CrossRef](#)]
138. Zeng, Y.; Zhong, J.; Wang, H.; Fu, M.; Ye, D.; Hu, Y. Synergistic effect of tunable oxygen-vacancy defects and graphene on accelerating the photothermal degradation of methanol over Co₃O₄/rGO nanocomposites. *Chem. Eng. J.* **2021**, *425*, 131658. [[CrossRef](#)]
139. Pang, Y.; Kong, L.; Lei, H.; Chen, D.; Yuvaraja, G. Combined microwave-induced and photocatalytic oxidation using zinc ferrite catalyst for efficient degradation of tetracycline hydrochloride in aqueous solution. *J. Taiwan Inst. Chem. E* **2018**, *93*, 397–404. [[CrossRef](#)]
140. Barik, A.J.; Kulkarni, S.V.; Gogate, P.R. Degradation of 4-chloro 2-aminophenol using combined approaches based on microwave and photocatalysis. *Sep. Purif. Technol.* **2016**, *168*, 152–160. [[CrossRef](#)]
141. Liu, X.; Chen, T.; Xue, Y.; Fan, J.; Shen, S.; Hossain, M.S.A.; Amin, M.A.; Pan, L.; Xu, X.; Yamauchi, Y. Nanoarchitectonics of MXene/semiconductor heterojunctions toward artificial photosynthesis via photocatalytic CO₂ reduction. *Coordin. Chem. Rev.* **2022**, *459*, 214440. [[CrossRef](#)]
142. Zhou, Y.; Wang, Z.; Huang, L.; Zaman, S.; Lei, K.; Yue, T.; Li, Z.A.; You, B.; Xia, B.Y. Engineering 2D Photocatalysts toward Carbon Dioxide Reduction. *Adv. Energy Mater.* **2021**, *11*, 2003159. [[CrossRef](#)]
143. Yamaguchi, Y.; Kudo, A. Visible light responsive photocatalysts developed by substitution with metal cations aiming at artificial photosynthesis. *Front. Energy* **2021**, *15*, 568–576. [[CrossRef](#)]
144. Fajrina, N.; Tahir, M. A critical review in strategies to improve photocatalytic water splitting towards hydrogen production. *Int. J. Hydrogen Energy* **2019**, *44*, 540–577. [[CrossRef](#)]
145. Tahir, M.; Tasleem, S.; Tahir, B. Recent development in band engineering of binary semiconductor materials for solar driven photocatalytic hydrogen production. *Int. J. Hydrogen Energy* **2020**, *45*, 15985–16038. [[CrossRef](#)]
146. Gopinath, C.S.; Nalajala, N. A scalable and thin film approach for solar hydrogen generation: A review on enhanced photocatalytic water splitting. *J. Mater. Chem. A* **2021**, *9*, 1353–1371. [[CrossRef](#)]
147. Zheng, H.; Li, X.; Zhu, K.; Liang, P.; Wu, M.; Rao, Y.; Jian, R.; Shi, F.; Wang, J.; Yan, K.; et al. Semiconducting BaTiO₃@C core-shell structure for improving piezo-photocatalytic performance. *Nano Energy* **2022**, *93*, 106831. [[CrossRef](#)]
148. Shi, J.; Xie, Z.; Tang, X.; Wang, Y.; Yuan, G.; Liu, J.-M. Enhanced piezo-photocatalytic performance of Ag@Na_{0.5}Bi_{0.5}TiO₃ composites. *J. Alloys Compd.* **2022**, *911*, 164885. [[CrossRef](#)]
149. Shen, W.; Li, N.; Zuo, S.; Wu, M.; Sun, G.; Li, Q.; Shi, M.; Ma, J. Remarkably enhanced piezo-photocatalytic performance of Z-scheme Bi₂WO₆/Black TiO₂ heterojunction via piezoelectric effect. *Ceram. Int.* **2022**, *48*, 15899–15907. [[CrossRef](#)]
150. Kang, Z.; Ke, K.; Lin, E.; Qin, N.; Wu, J.; Huang, R.; Bao, D. Piezoelectric polarization modulated novel Bi₂WO₆/g-C₃N₄/ZnO Z-scheme heterojunctions with g-C₃N₄ intermediate layer for efficient piezo-photocatalytic decomposition of harmful organic pollutants. *J. Colloid Interface Sci.* **2022**, *607*, 1589–1602. [[CrossRef](#)]
151. Gotipamul, P.P.; Vattikondala, G.; Rajan, K.D.; Khanna, S.; Rathinam, M.; Chidambaram, S. Impact of piezoelectric effect on the heterogeneous visible photocatalysis of g-C₃N₄/Ag/ZnO tricomponent. *Chemosphere* **2022**, *287*, 132298. [[CrossRef](#)] [[PubMed](#)]
152. Ding, D.; Li, Z.; Yu, S.; Yang, B.; Yin, Y.; Zan, L.; Myung, N.V. Piezo-photocatalytic flexible PAN/TiO₂ composite nanofibers for environmental remediation. *Sci. Total Environ.* **2022**, *824*, 153790. [[CrossRef](#)] [[PubMed](#)]
153. Xu, T.; Niu, P.; Wang, S.; Li, L. High visible light photocatalytic activities obtained by integrating g-C₃N₄ with ferroelectric PbTiO₃. *J. Mater. Sci. Technol.* **2021**, *74*, 128–135. [[CrossRef](#)]
154. Sun, H.; Xu, Z.; Xie, X.; Niu, J.; Wang, M.; Zhang, X.; Chen, X.; Han, J. Enhanced photocatalytic activity of ferroelectric-based Ag₂O/Bi₄Ti₃O₁₂ hybrids by piezoelectric effect. *J. Alloys Compd.* **2021**, *882*, 160609. [[CrossRef](#)]
155. Liu, X.; Shen, X.; Sa, B.; Zhang, Y.; Li, X.; Xue, H. Piezotronic-enhanced photocatalytic performance of heterostructured BaTiO₃/SrTiO₃ nanofibers. *Nano Energy* **2021**, *89*, 106391. [[CrossRef](#)]
156. Liu, J.; Chen, J.; Wu, Z.; Zhu, K.; Wang, J.; Li, Z.; Tai, G.; Liu, X.; Lu, S. Enhanced visible-light photocatalytic performances of ZnO through loading AgI and coupling piezo-photocatalysis. *J. Alloys Compd.* **2021**, *852*, 156848. [[CrossRef](#)]

157. Lei, H.; Wu, M.; Liu, Y.; Mo, F.; Chen, J.; Ji, S.; Zou, Y.; Dong, X. Built-in piezoelectric field improved photocatalytic performance of nanoflower-like Bi₂WO₆ using low-power white LEDs. *Chin. Chem. Lett.* **2021**, *32*, 2317–2321.
158. Jiang, X.; Wang, H.; Wang, X.; Yuan, G. Synergetic effect of piezoelectricity and Ag deposition on photocatalytic performance of barium titanate perovskite. *Sol. Energy* **2021**, *224*, 455–461. [[CrossRef](#)]
159. Dilly Rajan, K.; Gotipamul, P.P.; Khanna, S.; Chidambaram, S.; Rathinam, M. Piezo-photocatalytic effect of NaNbO₃ interconnected nanoparticles decorated CuBi₂O₄ nanocuboids. *Mater. Lett.* **2021**, *296*, 129902. [[CrossRef](#)]
160. Wu, J.; Wang, W.; Tian, Y.; Song, C.; Qiu, H.; Xue, H. Piezotronic effect boosted photocatalytic performance of heterostructured BaTiO₃/TiO₂ nanofibers for degradation of organic pollutants. *Nano Energy* **2020**, *77*, 105122.
161. Wu, W.; Yin, X.; Dai, B.; Kou, J.; Ni, Y.; Lu, C. Water flow driven piezo-photocatalytic flexible films: Bi-piezoelectric integration of ZnO nanorods and PVDF. *Appl. Surf. Sci.* **2020**, *517*, 146119. [[CrossRef](#)]
162. Ren, Z.; Li, X.; Guo, L.; Wu, J.; Li, Y.; Liu, W.; Li, P.; Fu, Y.; Ma, J. Facile synthesis of ZnO/ZnS heterojunction nanoarrays for enhanced piezo-photocatalytic performance. *Mater. Lett.* **2021**, *292*, 129635. [[CrossRef](#)]
163. Dursun, S.; Akyildiz, H.; Kalem, V. PMN-PT nanoparticle/SnO₂ nanofiber heterostructures: Enhanced photocatalytic degradation performance by ultrasonic wave induced piezoelectric field. *J. Alloys Compd.* **2021**, *889*, 161769. [[CrossRef](#)]
164. Cheng, T.; Gao, H.; Li, R.; Wang, S.; Yi, Z.; Yang, H. Flexoelectricity-induced enhancement in carrier separation and photocatalytic activity of a photocatalyst. *Appl. Surf. Sci.* **2021**, *566*, 150669. [[CrossRef](#)]
165. Yu, Y.; Yao, B.; He, Y.; Cao, B.; Ren, Y.; Sun, Q. Piezo-enhanced photodegradation of organic pollutants on Ag₃PO₄/ZnO nanowires using visible light and ultrasonic. *Appl. Surf. Sci.* **2020**, *528*, 146819. [[CrossRef](#)]
166. Fu, Y.; Wang, Y.; Zhao, H.; Zhang, Z.; An, B.; Bai, C.; Ren, Z.; Wu, J.; Li, Y.; Liu, W.; et al. Synthesis of ternary ZnO/ZnS/MoS₂ piezoelectric nanoarrays for enhanced photocatalytic performance by conversion of dual heterojunctions. *Appl. Surf. Sci.* **2021**, *556*, 149695. [[CrossRef](#)]
167. Yu, C.; Tan, M.; Tao, C.; Hou, Y.; Liu, C.; Meng, H.; Su, Y.; Qiao, L.; Bai, Y. Remarkably enhanced piezo-photocatalytic performance in BaTiO₃/CuO heterostructures for organic pollutant degradation. *J. Adv. Ceram.* **2022**, *11*, 414–426. [[CrossRef](#)]
168. Zhou, X.; Yan, F.; Wu, S.; Shen, B.; Zeng, H.; Zhai, J. Remarkable Piezophoto Coupling Catalysis Behavior of BiOX/BaTiO₃ (X = Cl, Br, Cl_{0.166}Br_{0.834}) Piezoelectric Composites. *Small* **2020**, *16*, e2001573. [[CrossRef](#)]
169. Wang, R.; Xie, X.; Xu, C.; Lin, Y.; You, D.; Chen, J.; Li, Z.; Shi, Z.; Cui, Q.; Wang, M. Bi-piezoelectric effect assisted ZnO nanorods/PVDF-HFP spongy photocatalyst for enhanced performance on degrading organic pollutant. *Chem. Eng. J.* **2022**, *439*, 135787. [[CrossRef](#)]
170. Fu, Y.; Ren, Z.; Wu, J.; Li, Y.; Liu, W.; Li, P.; Xing, L.; Ma, J.; Wang, H.; Xue, X. Direct Z-scheme heterojunction of ZnO/MoS₂ nanoarrays realized by flowing-induced piezoelectric field for enhanced sunlight photocatalytic performances. *Appl. Catal. B Environ.* **2021**, *285*, 119785. [[CrossRef](#)]
171. Tong, W.; Zhang, Y.; Huang, H.; Xiao, K.; Yu, S.; Zhou, Y.; Liu, L.; Li, H.; Liu, L.; Huang, T.; et al. A highly sensitive hybridized soft piezophotocatalyst driven by gentle mechanical disturbances in water. *Nano Energy* **2018**, *53*, 513–523. [[CrossRef](#)]
172. Yao, Z.; Sun, H.; Xiao, S.; Hu, Y.; Liu, X.; Zhang, Y. Synergetic piezo-photocatalytic effect in a Bi₂MoO₆/BiOBr composite for decomposing organic pollutants. *Appl. Surf. Sci.* **2021**, *560*, 150037. [[CrossRef](#)]
173. Zhu, Q.; Dar, A.A.; Zhou, Y.; Zhang, K.; Qin, J.; Pan, B.; Lin, J.; Patrocínio, A.O.T.; Wang, C. Oxygen Vacancies Promoted Piezoelectricity toward Piezo-Photocatalytic Decomposition of Tetracycline over SrBi₄Ti₄O₁₅. *ACS EST Eng.* **2022**, *2*, 1365–1375. [[CrossRef](#)]
174. Zhou, L.; Dai, S.; Xu, S.; She, Y.; Li, Y.; Leveueur, S.; Qin, Y. Piezoelectric effect synergistically enhances the performance of Ti₃₂-oxo-cluster/BaTiO₃/CuS p-n heterojunction photocatalytic degradation of pollutants. *Appl. Catal. B Environ.* **2021**, *291*, 120019. [[CrossRef](#)]
175. Chen, J.; Liao, B.; Liao, X.; Xie, H.; Yu, Y.; Hou, S.; Wang, C.; Fan, X. Strain-Driven Polarized Electric Field-Promoted Photocatalytic Activity in Borate-Based CsCdBO₃ Bulk Materials. *ACS Appl. Mater. Interfaces* **2021**, *13*, 34202–34212. [[CrossRef](#)]
176. Zhang, C.; Li, N.; Chen, D.; Xu, Q.; Li, H.; He, J.; Lu, J. The ultrasonic-induced-piezoelectric enhanced photocatalytic performance of ZnO/CdS nanofibers for degradation of bisphenol A. *J. Alloys Compd.* **2021**, *885*, 160987. [[CrossRef](#)]
177. Zhang, C.; Fei, W.; Wang, H.; Li, N.; Chen, D.; Xu, Q.; Li, H.; He, J.; Lu, J. p-n Heterojunction of BiOI/ZnO nanorod arrays for piezo-photocatalytic degradation of bisphenol A in water. *J. Hazard. Mater.* **2020**, *399*, 123109. [[CrossRef](#)]
178. Feng, Y.; Li, H.; Ling, L.; Yan, S.; Pan, D.; Ge, H.; Li, H.; Bian, Z. Enhanced Photocatalytic Degradation Performance by Fluid-Induced Piezoelectric Field. *Environ. Sci. Technol.* **2018**, *52*, 7842–7848. [[CrossRef](#)]
179. Hu, J.; Chen, Y.; Zhou, Y.; Zeng, L.; Huang, Y.; Lan, S.; Zhu, M. Piezo-enhanced charge carrier separation over plasmonic Au-BiOBr for piezo-photocatalytic carbamazepine removal. *Appl. Catal. B Environ.* **2022**, *311*, 121369. [[CrossRef](#)]
180. Li, Y.; Li, R.; Zhai, Y.; Huang, Y.; Lee, S.; Cao, J. Improved photocatalytic activity of BaTiO₃/La₂Ti₂O₇ heterojunction composites via piezoelectric-enhanced charge transfer. *Appl. Surf. Sci.* **2021**, *570*, 151146. [[CrossRef](#)]
181. Li, M.; Sun, J.; Chen, G.; Yao, S.; Cong, B. Construction double electric field of sulphur vacancies as medium ZnS/Bi₂S₃-PVDF self-supported recoverable piezoelectric film photocatalyst for enhanced photocatalytic performance. *Appl. Catal. B Environ.* **2022**, *301*, 120792. [[CrossRef](#)]
182. Jiang, Y.; Xie, J.; Lu, Z.; Hu, J.; Hao, A.; Cao, Y. Insight into the effect of OH modification on the piezo-photocatalytic hydrogen production activity of SrTiO₃. *J. Colloid Interface Sci.* **2022**, *612*, 111–120. [[CrossRef](#)]

183. Huang, X.; Lei, R.; Yuan, J.; Gao, F.; Jiang, C.; Feng, W.; Zhuang, J.; Liu, P. Insight into the piezo-photo coupling effect of PbTiO₃/CdS composites for piezo-photocatalytic hydrogen production. *Appl. Catal. B Environ.* **2021**, *282*, 119586. [CrossRef]
184. Hu, C.; Chen, F.; Wang, Y.; Tian, N.; Ma, T.; Zhang, Y.; Huang, H. Exceptional Cocatalyst-Free Photo-Enhanced Piezocatalytic Hydrogen Evolution of Carbon Nitride Nanosheets from Strong In-Plane Polarization. *Adv. Mater.* **2021**, *33*, e2101751. [CrossRef]
185. Cui, Y.; Wang, Z.; Li, B.; Yan, Y.; Xu, R.; Meng, M.; Yan, Y. Fluid-induced piezoelectric field enhancing photocatalytic hydrogen evolution reaction on g-C₃N₄/LiNbO₃/PVDF membrane. *Nano Energy* **2022**, *99*, 107429. [CrossRef]
186. Tang, R.; Gong, D.; Zhou, Y.; Deng, Y.; Feng, C.; Xiong, S.; Huang, Y.; Peng, G.; Li, L.; Zhou, Z. Unique g-C₃N₄/PDI-g-C₃N₄ homojunction with synergistic piezo-photocatalytic effect for aquatic contaminant control and H₂O₂ generation under visible light. *Appl. Catal. B Environ.* **2022**, *303*, 120929. [CrossRef]
187. Zhou, X.; Shen, B.; Zhai, J.; Conesa, J.C. High Performance Generation of H₂O₂ under Piezophototronic Effect with Multi-Layer In₂S₃ Nanosheets Modified by Spherical ZnS and BaTiO₃ Nanopiezoelectrics. *Small Methods* **2021**, *5*, e2100269. [CrossRef] [PubMed]
188. Mohanty, R.; Mansingh, S.; Parida, K.; Parida, K. Boosting sluggish photocatalytic hydrogen evolution through piezo-stimulated polarization: A critical review. *Mater. Horiz.* **2022**, *9*, 1332–1355. [CrossRef]
189. Yan, X.; Li, G.; Wang, Z.; Yu, Z.; Wang, K.; Wu, Y. Recent progress on piezoelectric materials for renewable energy conversion. *Nano Energy* **2020**, *77*, 105180. [CrossRef]
190. Pan, L.; Sun, S.; Chen, Y.; Wang, P.; Wang, J.; Zhang, X.; Zou, J.J.; Wang, Z.L. Advances in Piezo-Phototronic Effect Enhanced Photocatalysis and Photoelectrocatalysis. *Adv. Energy Mater.* **2020**, *10*, 2000214. [CrossRef]
191. Liu, Z.; Yu, X.; Li, L. Piezopotential augmented photo- and photoelectro-catalysis with a built-in electric field. *Chin. J. Catal.* **2020**, *41*, 534–549. [CrossRef]
192. Lops, C.; Ancona, A.; Di Cesare, K.; Dumontel, B.; Garino, N.; Canavese, G.; Hernandez, S.; Cauda, V. Sonophotocatalytic degradation mechanisms of Rhodamine B dye via radicals generation by micro- and nano-particles of ZnO. *Appl. Catal. B Environ.* **2019**, *243*, 629–640. [CrossRef] [PubMed]
193. Li, H.; Sang, Y.; Chang, S.; Huang, X.; Zhang, Y.; Yang, R.; Jiang, H.; Liu, H.; Wang, Z.L. Enhanced ferroelectric-nanocrystal-based hybrid photocatalysis by ultrasonic-wave-generated piezophototronic effect. *Nano Lett.* **2015**, *15*, 2372–2379. [CrossRef] [PubMed]
194. Xu, S.; Guo, L.; Sun, Q.; Wang, Z.L. Piezotronic Effect Enhanced Plasmonic Photocatalysis by AuNPs/BaTiO₃ Heterostructures. *Adv. Funct. Mater.* **2019**, *29*, 1808737. [CrossRef]
195. Liu, Q.; Zhao, W.; Ao, Z.; An, T. Photo-piezoelectric synergistic degradation of typical volatile organic compounds on BaTiO₃. *Chin. Chem. Lett.* **2022**, *33*, 410–414. [CrossRef]
196. Jiang, Y.; Li, M.; Mi, Y.; Guo, L.; Fang, W.; Zeng, X.; Zhou, T.; Liu, Y. The influence of piezoelectric effect on the heterogeneous photocatalytic hydrogen production of strontium titanate nanoparticles. *Nano Energy* **2021**, *85*, 105949. [CrossRef]
197. Zhao, J.; Yang, H.; Li, Y.; Lu, K. Photocatalytic activity of CdS nanoparticles enhanced by the interaction between piezotronic effect and phase junction. *J. Alloys Compd.* **2020**, *815*, 152494. [CrossRef]
198. Zhao, Y.; Huang, X.; Gao, F.; Zhang, L.; Tian, Q.; Fang, Z.B.; Liu, P. Study on water splitting characteristics of CdS nanosheets driven by the coupling effect between photocatalysis and piezoelectricity. *Nanoscale* **2019**, *11*, 9085–9090. [CrossRef]
199. Li, Y.; Wang, Q.; Wang, H.; Tian, J.; Cui, H. Novel Ag₂O nanoparticles modified MoS₂ nanoflowers for piezoelectric-assisted full solar spectrum photocatalysis. *J. Colloid Interface Sci.* **2019**, *537*, 206–214. [CrossRef]
200. Chou, T.-M.; Chan, S.-W.; Lin, Y.-J.; Yang, P.-K.; Liu, C.-C.; Lin, Y.-J.; Wu, J.-M.; Lee, J.-T.; Lin, Z.-H. A highly efficient Au-MoS₂ nanocatalyst for tunable piezocatalytic and photocatalytic water disinfection. *Nano Energy* **2019**, *57*, 14–21. [CrossRef]
201. Venkatesan, M.; Chen, W.-C.; Cho, C.-J.; Veeramuthu, L.; Chen, L.-G.; Li, K.-Y.; Tsai, M.-L.; Lai, Y.-C.; Lee, W.-Y.; Chen, W.-C.; et al. Enhanced piezoelectric and photocatalytic performance of flexible energy harvester based on CsZn_{0.75}Pb_{0.25}I₃/CNC-PVDF composite nanofibers. *Chem. Eng. J.* **2022**, *433*, 133620. [CrossRef]
202. Pan, J.; Li, Y.; Guo, G.; Zhao, X.; Yu, J.; Li, Z.; Xu, S.; Man, B.; Wei, D.; Zhang, C. Synergizing piezoelectric and plasmonic modulation of PVDF/MoS₂ cavity/Au for enhanced photocatalysis. *Appl. Surf. Sci.* **2022**, *577*, 151811. [CrossRef]
203. Sittipol, W.; Sronsri, C.; U-yen, K. Effect of magnetic fields on the efficiency of the photocatalytic degradation of methylene blue in a dynamic fluid system. *J. Clean Prod.* **2021**, *325*, 129284. [CrossRef]
204. Silva, E.C.; Bonacin, J.A.; Passos, R.R.; Pocrifka, L.A. The effect of an external magnetic field on the photocatalytic activity of CoFe₂O₄ particles anchored in carbon cloth. *J. Photoch. Photobio. A* **2021**, *416*, 113317. [CrossRef]
205. Tank, C.M.; Sakhare, Y.S.; Kanhe, N.S.; Nawale, A.B.; Das, A.K.; Bhoraskar, S.V.; Mathe, V.L. Electric field enhanced photocatalytic properties of TiO₂ nanoparticles immobilized in porous silicon template. *Solid State Sci.* **2011**, *13*, 1500–1504. [CrossRef]
206. Gao, W.; Zhao, X.; Cui, C.; Su, X.; Zhang, S.; Wang, X.; Zhang, X.L.; Sang, Y.; Liu, H. High-efficiency separation and transfer of photo-induced charge carrier in graphene/TiO₂ via heterostructure in magnetic field. *J. Alloys Compd.* **2021**, *862*, 158283. [CrossRef]
207. Bian, Y.; Zheng, G.; Ding, W.; Hu, L.; Sheng, Z. Magnetic field effect on the photocatalytic degradation of methyl orange by commercial TiO₂ powder. *RSC Adv.* **2021**, *11*, 6284–6291. [CrossRef]
208. Zhao, C.; Zhou, L.; Zhang, Z.; Gao, Z.; Weng, H.; Zhang, W.; Li, L.; Song, Y.Y. Insight of the Influence of Magnetic-Field Direction on Magneto-Plasmonic Interfaces for Tuning Photocatalytical Performance of Semiconductors. *J. Phys. Chem. Lett.* **2020**, *11*, 9931–9937. [CrossRef]

209. Pan, L.; Ai, M.; Huang, C.; Yin, L.; Liu, X.; Zhang, R.; Wang, S.; Jiang, Z.; Zhang, X.; Zou, J.J.; et al. Manipulating spin polarization of titanium dioxide for efficient photocatalysis. *Nat. Commun.* **2020**, *11*, 418. [[CrossRef](#)]
210. Huang, G.; Zhang, G.; Gao, Z.; Cao, J.; Li, D.; Yun, H.; Zeng, T. Enhanced visible-light-driven photocatalytic activity of BiFeO₃ via electric-field control of spontaneous polarization. *J. Alloys Compd.* **2019**, *783*, 943–951. [[CrossRef](#)]
211. Wang, Y.; Wang, S.; Wu, Y.; Wang, Z.; Zhang, H.; Cao, Z.; He, J.; Li, W.; Yang, Z.; Zheng, L.; et al. A α -Fe₂O₃/rGO magnetic photocatalyst: Enhanced photocatalytic performance regulated by magnetic field. *J. Alloys Compd.* **2021**, *851*, 156733. [[CrossRef](#)]
212. Lu, Y.; Ren, B.; Chang, S.; Mi, W.; He, J.; Wang, W. Achieving effective control of the photocatalytic performance for CoFe₂O₄/MoS₂ heterojunction via exerting external magnetic fields. *Mater. Lett.* **2020**, *260*, 126979. [[CrossRef](#)]
213. Huang, H.; Chen, Y.; Shi, H. Boosting Separation of Charge Carriers in 2D/0D BiOBr Nanoflower Sheets/BN Quantum Dots with the Lorentz Force via Magnetic Field. *Energ. Fuel* **2022**. [[CrossRef](#)]
214. Zhao, Y.; Huang, Z.; Chang, W.; Wei, C.; Feng, X.; Ma, L.; Qi, X.; Li, Z. Microwave-assisted solvothermal synthesis of hierarchical TiO₂ microspheres for efficient electro-field-assisted-photocatalytic removal of tributyltin in tannery wastewater. *Chemosphere* **2017**, *179*, 75–83. [[CrossRef](#)]
215. Li, N.; He, M.; Lu, X.; Liang, L.; Li, R.; Yan, B.; Chen, G. Enhanced norfloxacin degradation by visible-light-driven Mn₃O₄/gamma-MnOOH photocatalysis under weak magnetic field. *Sci. Total Environ.* **2021**, *761*, 143268. [[CrossRef](#)]
216. Wu, Y.; Li, T.; Ren, X.; Fu, Y.; Zhang, H.; Feng, X.; Huang, H.; Xie, R. Magnetic field assisted alpha-Fe₂O₃/Zn_{1-x}Fe_xO heterojunctions for accelerating antiviral agents degradation under visible-light. *J. Environ. Chem. Eng.* **2022**, *10*, 106990. [[CrossRef](#)]
217. Li, Y.; Wang, Z.; Wang, Y.; Kovács, A.; Foo, C.; Dunin-Borkowski, R.E.; Lu, Y.; Taylor, R.A.; Wu, C.; Tsang, S.C.E. Local magnetic spin mismatch promoting photocatalytic overall water splitting with exceptional solar-to-hydrogen efficiency. *Energy Environ. Sci.* **2022**, *15*, 265–277. [[CrossRef](#)]
218. Zhao, X.; Gao, W.; Liu, Q.; Cui, C.; Zhou, W.; Wang, X.; Zhang, X.L.; Zhao, L.; Sang, Y.; Liu, H. Enhanced photo-induced carrier separation of CdS/MoS₂ via micro-potential of Mo microsheet derived from electromagnetic induction. *Chem. Eng. J.* **2021**, *404*, 126972. [[CrossRef](#)]
219. Gao, W.; Liu, Q.; Zhang, S.; Yang, Y.; Zhang, X.; Zhao, H.; Qin, W.; Zhou, W.; Wang, X.; Liu, H.; et al. Electromagnetic induction derived micro-electric potential in metal-semiconductor core-shell hybrid nanostructure enhancing charge separation for high performance photocatalysis. *Nano Energy* **2020**, *71*, 104624. [[CrossRef](#)]
220. Pan, H.; Sun, M.; Wang, X.; Zhang, M.; Murugananthan, M.; Zhang, Y. A novel electric-assisted photocatalytic technique using self-doped TiO₂ nanotube films. *Appl. Catal. B Environ.* **2022**, *307*, 121174. [[CrossRef](#)]
221. Park, S.; Lee, C.W.; Kang, M.-G.; Kim, S.; Kim, H.J.; Kwon, J.E.; Park, S.Y.; Kang, C.-Y.; Hong, K.S.; Nam, K.T. A ferroelectric photocatalyst for enhancing hydrogen evolution: Polarized particulate suspension. *Phys. Chem. Chem. Phys.* **2014**, *16*, 10408–10413. [[CrossRef](#)] [[PubMed](#)]
222. Xu, S.C.; Ding, H.L.; Pan, S.S.; Luo, Y.Y.; Li, G.H. Electric-Field-Enhanced Photocatalytic Removal of Cr(VI) under Sunlight of TiO₂ Nanograss Mesh with Nondestructive Regeneration and Feasible Collection for Cr(III). *Acs Sustain. Chem. Eng.* **2016**, *4*, 6887–6893. [[CrossRef](#)]
223. Li, S.; Bai, L.; Ji, N.; Yu, S.; Lin, S.; Tian, N.; Huang, H. Ferroelectric polarization and thin-layered structure synergistically promoting CO₂ photoreduction of Bi₂MoO₆. *J. Mater. Chem. A* **2020**, *8*, 9268–9277. [[CrossRef](#)]
224. Zhao, Z.; Wang, D.; Gao, R.; Wen, G.; Feng, M.; Song, G.; Zhu, J.; Luo, D.; Tan, H.; Ge, X.; et al. Magnetic-Field-Stimulated Efficient Photocatalytic N₂ Fixation over Defective BaTiO₃ Perovskites. *Angew. Chem. Int. Ed.* **2021**, *60*, 11910–11918. [[CrossRef](#)]
225. Gao, W.; Lu, J.; Zhang, S.; Zhang, X.; Wang, Z.; Qin, W.; Wang, J.; Zhou, W.; Liu, H.; Sang, Y. Suppressing Photoinduced Charge Recombination via the Lorentz Force in a Photocatalytic System. *Adv. Sci.* **2019**, *6*, 1901244. [[CrossRef](#)]
226. Zhao, J.; Li, N.; Yu, R.; Zhao, Z.; Nan, J. Magnetic field enhanced denitrification in nitrate and ammonia contaminated water under 3D/2D Mn₂O₃/g-C₃N₄ photocatalysis. *Chem. Eng. J.* **2018**, *349*, 530–538. [[CrossRef](#)]
227. Peng, C.; Fan, W.; Li, Q.; Han, W.; Chen, X.; Zhang, G.; Yan, Y.; Gu, Q.; Wang, C.; Zhang, H.; et al. Boosting photocatalytic activity through tuning electron spin states and external magnetic fields. *J. Mater. Sci. Technol.* **2022**, *115*, 208–220. [[CrossRef](#)]